nature communications

Article

https://doi.org/10.1038/s41467-024-54287-x

Rational design of uncleaved prefusion-closed trimer vaccines for human respiratory syncytial virus and metapneumovirus

Received: 12 March 2024

Accepted: 4 November 2024

Published online: 16 November 2024

Check for updates

Yi-Zong Lee[1,5], Jerome Han[1,5], Yi-Nan Zhang[1,5], Garrett Ward[1], Keegan Braz Gomes[2], Sarah Auclair[1], Robyn L. Stanfield[1], Linling He[1], Ian A. Wilson[1,3] & Jiang Zhu[1,2,4]

Respiratory syncytial virus (RSV) and human metapneumovirus (hMPV) cause human respiratory diseases and are major targets for vaccine development. In this study, we design uncleaved prefusion-closed (UFC) trimers for the fusion protein (F) of both viruses by examining mutations critical to F metastability. For RSV, we assess four previous prefusion F designs, including the first and second generations of DS-Cav1, SC-TM, and 847A. We then identify key mutations that can maintain prefusion F in a native-like, closed trimeric form (up to 76%) without introducing any interprotomer disulfide bond. For hMPV, we develop a stable UFC trimer with a truncated F_2-F_1 linkage and an interprotomer disulfide bond. Dozens of UFC constructs are characterized by negative-stain electron microscopy (nsEM), x-ray crystallography (11 RSV-F structures and one hMPV-F structure), and antigenic profiling. Using an optimized RSV-F UFC trimer as bait, we identify three potent RSV neutralizing antibodies (NAbs) from a phage-displayed human antibody library, with a public NAb lineage targeting sites Ø and V and two cross-pneumovirus NAbs recognizing site III. In mouse immunization, rationally designed RSV-F and hMPV-F UFC trimers induce robust antibody responses with high neutralizing titers. Our study provides a foundation for future prefusion F-based RSV and hMPV vaccine development.

Respiratory syncytial virus (RSV) and human metapneumovirus (hMPV) pose a significant threat to public health worldwide[1,2]. RSV is a major cause of lower respiratory tract (LRT) infections in infants, young children, the elderly, and immunocompromised individuals[3–6]. The recently discovered hMPV affects the same populations[7–12], causing upper and lower respiratory tract infections in mostly young children and individuals who suffer from asthma, pulmonary diseases, and cancer[13–17]. Furthermore, hMPV is capable of coinfections with other respiratory viruses, including RSV[11,18,19], thus increasing mortality and morbidity in young children[20]. Both RSV and hMPV are enveloped, non-segmented, negative-sense, single-stranded RNA viruses of the *Pneumoviridae* family[1,2]. Their viral genomes encode three surface proteins: glycoprotein (G) that is responsible for viral attachment to cell surface factors, fusion protein (F), which fuses viral and host cell membranes during viral entry[21,22], and small hydrophobic (SH) protein, which is a viroporin. Although both G and F can be recognized by host neutralizing antibodies (NAbs) during natural infection[23–26], F is highly conserved among subtypes and

[1]Department of Integrative Structural and Computational Biology, The Scripps Research Institute, La Jolla, CA 92037, USA. [2]Uvax Bio, LLC, Newark, DE 19702, USA. [3]Skaggs Institute for Chemical Biology, The Scripps Research Institute, La Jolla, CA 92037, USA. [4]Department of Immunology and Microbiology, The Scripps Research Institute, La Jolla, CA 92037, USA. [5]These authors contributed equally: Yi-Zong Lee, Jerome Han, Yi-Nan Zhang.
e-mail: jiang@scripps.edu

represents a primary target for both RSV and hMPV vaccine development[27,28].

RSV-F and hMPV-F are class I viral fusion glycoproteins with ~30% sequence identity. The two F proteins share many structural and functional similarities in their pre- and postfusion states, which have led to the design of a pan-pneumovirus F antigen[29]. To enable cell entry, the RSV-F precursor, F_0, is first cleaved by furin-like proteases at two sites to remove a 27-amino-acid (aa) peptide (p27)[30,31] and generate two subunits: an N-terminal F_2 that is attached to a larger C-terminal F_1 subunit by two disulfide bonds to form a heterodimer, three of which assemble into a functional trimer[27]. Some studies suggest that trimerization occurs after proteolytic activation[32,33], which would make RSV-F distinct from other class I fusion proteins, such as HIV-1 envelope glycoprotein (Env), but it is unclear whether this prefusion F trimer adopts a fully closed conformation on virions. For hMPV, proteolytic cleavage at a single site by serine proteases[34] transforms F_0 into F_2 and F_1 subunits, which form a functional prefusion hMPV-F trimer[35]. The metastable prefusion RSV-F and hMPV-F then undergo irreversible refolding, during which the hydrophobic fusion peptides are ejected from the central cavity of the F trimer and inserted into host cell membranes to facilitate virus-host membrane fusion and the rapid transition of F into a highly stable postfusion form[27,35]. An important lesson from decades of RSV vaccine research and clinical studies is that postfusion F elicits weak NAb or nonfunctional antibody responses with adverse effects, making it unsuitable for use as a vaccine antigen[36]. In contrast, prefusion F induces superior NAb responses accounting for most of the RSV-neutralizing activity in human immune sera[25,26]. Passive transfer of prefusion F-specific NAbs, including maternal transfer of such antibodies, may effectively prevent or treat RSV infection[37–39].

Structure-based antigen design has played an essential role in the development of prefusion RSV-F vaccines[40,41]. Three prefusion F-specific NAbs (D25, AM22, and 5C4) were key to the determination of the first prefusion RSV-F structure[42], which led to a breakthrough in the first prefusion-stabilized F design, DS-Cav1[43]. Based on the structural information, alternative designs were proposed to stabilize prefusion RSV-F in either cleaved or uncleaved forms[33,44,45]. Structures of prefusion RSV-F in complex with diverse NAbs[32,46–52] have defined six major antigenic sites, two of which (Ø and V) are prefusion-specific and can elicit NAbs that are 10–100 times more potent than those targeting sites (I, II, III, and IV) that are accessible in both pre- and postfusion states[36,53]. These studies paved the way for two approved RSV vaccines, ABRYSVO (GlaxoSmithKline [GSK])[54] and AREXVY (Pfizer)[55], as well as other vaccine candidates under preclinical and clinical development[56–58]. Notably, an mRNA vaccine showed 83.7% efficacy against RSV in older adults[59] that was comparable to an efficacy of 82.6–88.9% for the two marketed protein vaccines. For hMPV, similar design strategies (e.g., disulfide bond, proline, and cavity-filling substitutions) have recently been used to stabilize prefusion F for vaccine development[35,60–62]. In addition to 101F and MPE8, which are previously identified NAbs targeting both RSV and hMPV[63,64], diverse hMPV NAbs have now been identified and structurally characterized using prefusion F[65–67]. Although these prefusion hMPV-F constructs showed promising results in animal studies[60,61], significant gaps remain between preclinical research and vaccine approval for human use. Nevertheless, structure-based rational antigen design will likely also be the driving force for hMPV vaccine development, as it has been for RSV.

Recently, we established a rational vaccine strategy for class-I viral fusion glycoproteins based on the analysis of their metastability[68–71]. Such analyses were proposed to lead to general design principles applicable to diverse subtypes within the virus family to stabilize their surface antigens in a native-like, prefusion state. We also found that the causes of metastability could be encoded by different regions in the fusion domain. For HIV-1 Env, the N-terminal bend of heptad repeat 1 ($HR1_N$) in gp41 was identified as the major cause of metastability[70,71], whereas for Ebola virus (EBOV) glycoprotein (GP) and SARS-CoV-2 spike, the long stalk in GP2 and triple hinged HR2 in S2 were key contributors to metastability, respectively. Notably, metastability may have different forms. Although wildtype and early-generation uncleaved HIV-1 Env constructs yielded non-native trimers[72–74], the unmutated EBOV GP with the mucin deletion (GPΔmuc) could not be retained as a closed trimer[69]. For RSV-F and hMPV-F, the strong tendency to undergo a rapid pre- to postfusion conformational rearrangement represents a distinct form of metastability. A recent study reported antibody-induced transient opening of the prefusion RSV-F trimer, suggesting another form of metastability[50]. Although diverse designs have been reported to stabilize prefusion RSV-F[33,43–45] and hMPV-F[35,60–62], the causes of metastability have largely remained unclear for these two pneumovirus fusion proteins.

In this study, we designed prefusion RSV-F and hMPV-F based on metastability analysis. Negative-stain electron microscopy (nsEM) and x-ray crystallography were utilized to structurally characterize F proteins in addition to extensive biochemical, biophysical, and antigenic analyses. As controls, we first evaluated previously reported RSV-F designs: DS-Cav1[43], SC-TM[33], sc9-10 DS-Cav1[44], and 847A[45], with and without a His_6 tag. We next designed and assessed, under the same experimental conditions as for the controls, uncleaved prefusion-closed (UFC) RSV-F trimers derived from three "base" constructs termed $UFC_{R1\text{-}3}$. Introducing hydrogen bonds or hydrophobic interactions to an occluded acidic patch (^{486}DEFD^{489}) situated above the trimeric coiled-coil stalk in F_1 substantially increased the ratio of prefusion-closed trimers from ~4% to 76% in solution. A total of 11 crystal structures were determined to verify our RSV-F designs. We then applied a similar design strategy to hMPV-F. Indeed, a slightly shortened F_2-F_1 linkage and a well-positioned interprotomer disulfide bond could effectively stabilize hMPV-F in a prefusion-closed trimer, confirmed by nsEM and a crystal structure at 6 Å resolution. To further evaluate these prefusion F constructs, we screened a human antibody library against an optimized RSV-F UFC trimer. Three potent NAbs were identified that shared the same epitopes as either the prefusion-specific NAb RSD5 targeting sites Ø and V[51], confirmed by nsEM and a 4.0 Å-resolution crystal structure, or the cross-pneumovirus NAb MPE8[63]. The NAb A4 shared the same germline genes as RSD5[51], thus defining a public antibody lineage. Lastly, we immunized mice with various RSV-F and hMPV-F constructs to evaluate their vaccine-induced antibody responses. In summary, the metastability analysis and UFC design strategy presented in this study will facilitate next-generation vaccine development for RSV and hMPV.

Results

Comparative analysis of previously reported prefusion RSV-F designs

Among four previously reported RSV-F designs (Fig. S1a, Table S1a), first-generation DS-Cav1 contains an engineered disulfide bond (S155C-S290C) in F_1 and two hydrophobic mutations (S190F/V207L)[43]. DS-Cav1 has been used to develop protein subunit, nanoparticle (NP), and mRNA vaccine candidates[58,59,75,76] and has inspired other RSV-F designs[33,44,45]. Unlike DS-Cav1, both SC-TM[33] and sc9-10 DS-Cav1[44] are uncleaved and connect F_2 and F_1 with a GS linker, in addition to a proline mutation (S215P). Sc9-10 DS-Cav1[44] also truncates the F_2 C-terminus, removes the fusion peptide (FP), and includes an interprotomer disulfide bond (A149C-Y458C). 847A[45] represents another cleaved RSV-F design, containing a disulfide bond (T103C-I148C) between F_2 and F_1 and a D486S mutation in the acidic patch (^{486}DEFD^{489}). A foldon trimerization motif was appended to the F_1 C-terminus (L513) with or without a His_6 tag, producing a total of eight constructs for four RSV-F designs.

For our experiments, all eight RSV-F constructs were transiently expressed in ExpiCHO cells and purified either by an immobilized nickel affinity (Nickel) column or by immunoaffinity chromatography

(IAC) using a site Ø-specific D25 antibody column[42]. The purified protein was then characterized using size exclusion chromatography (SEC), differential scanning calorimetry (DSC), and nsEM (Fig. S1b). For DS-Cav1[43], the SEC profiles from both Nickel and D25 affinity columns contained a major aggregate peak at 8-9 ml, while the former resulted in a larger trimer peak relative to the latter (Fig. 1a, left top). DS-Cav1-His_6 produced two peaks in the DSC thermogram, with the first and second melting temperatures (T_{m1} and T_{m2}) determined at 48.6 °C and 71.7 °C, respectively (Fig. 1a, left bottom). The nsEM analysis revealed that the Nickel/SEC-purified trimer peak contained only a small fraction of closed trimers among a large population of dissociated prefusion trimers (Fig. 1a, right); similar results were seen for the D25/SEC-purified sample (Fig. S1c, left). For SC-TM[33], D25 purification resulted in a negligible yield, whereas a Nickel column produced a large trimer peak, as well as visible aggregate and monomer peaks (Fig. 1b, left top). Nickel/SEC-purified SC-TM-His_6 was analyzed by DSC, which generated a similar double-peak thermograph with T_{m1} and T_{m2} determined at 50.7 °C and 61.4 °C, respectively (Fig. 1b, left bottom). In nsEM images, the Nickel/SEC-purified SC-TM-His_6 sample contained both open and closed trimers, as well as monomers (Fig. 1b, middle left). The 2D classification analysis indicated that ~28% of the trimers were in a prefusion-closed form, further confirmed by fitting the crystal structure of SC-TM (PDB ID: 5C6B) into the nsEM density map (Fig. 1b, middle right). However, postfusion F could also be observed in EM micrographs (Fig. 1b, right). For the third design, sc9-10 DS-Cav1[44], the two purification methods generated almost identical SEC profiles showing a single trimer peak with substantial yield and purity (Fig. 1c, left top). Greater thermostability was observed for Nickel/SEC-purified sc9-10 DS-Cav1-His_6 (Fig. 1c, left bottom), with T_{m1} and T_{m2} being ~10–20 °C higher than those of His-tagged DS-Cav1 and SC-TM. The nsEM analysis and structure fitting (PDB ID: 5K6I) indicated that sc9-10 DS-Cav1 contained ~100% prefusion-closed trimers regardless of the purification method used (Fig. 1c, middle; Fig. S1c, right), likely due to the interprotomer disulfide bond. The last RSV-F design, 847A[45], showed little to no trimer yield after D25 purification but produced notable trimer and monomer peaks after Nickel purification (Fig. 1d, left top). 847A-His_6 exhibited a unique DSC profile with a single T_m determined at 64.2 °C (Fig. 1d, left bottom), which is close to the T_{m1} of sc9-10 DS-Cav1-His_6. The nsEM analysis indicated that the closed trimer population was composed of both prefusion (~94%) and postfusion (~2%) F trimers (Fig. 1d, middle and right; Fig. S1d). The prefusion-closed form was confirmed by fitting the crystal structure of 847A (PDB ID: 7UJ3) into the nsEM density map (Fig. 1d, middle right). For the four His-tagged RSV-F constructs, the Nickel/SEC-purified trimer fractions were crosslinked using disuccinimidyl glutarate (DSG) and subjected to sodium dodecyl sulfate-polyacrylamide gel electrophoresis (SDS-PAGE) under reducing conditions (Fig. S1e). Regardless of the purification method used, His-tagged DS-Cav1, SC-TM, and 847A showed both trimer and monomer bands on the gel, as a fraction of open trimers that could not be cross-linked might be reduced to monomers under denaturing conditions. In contrast, a concentrated trimer band was observed for sc9-10 DS-Cav1-His_6.

Antigenicity was assessed using a panel of 10 antibodies targeting all major antigenic sites (defined in Fig. S1a), including D25, AM22, and 5C4 (site Ø)[42,46,51], ADI-14359 (site I)[48], motavizumab (site II)[32,77], MPE8 (site III)[63], 101F (site IV)[78], hRSV90 (site V)[47], AM14 (the IV-V interface)[32], and ADI-19425 (the III-IV interface)[48]. The four Nickel/SEC-purified RSV-F-His_6 samples, together with a D25/SEC-purified sc9-10 DS-Cav1 sample, were analyzed by enzyme-linked immunosorbent assay (ELISA) (Fig. 1e and Fig. S1f). His-tagged DS-Cav1, SC-TM, and sc9-10 DS-Cav1 bound to prefusion-specific, site Ø-directed NAbs with higher affinities than 847A-His_6, indicated by the half maximal effective concentration (EC_{50}). As expected, D25 purification resulted in an up to 2.1-fold improvement in EC_{50} for sc9-10 DS-Cav1 binding to NAb D25. Meanwhile, His-tagged SC-TM and 847A completely lost recognition by NAb AM22. Notably, His-tagged SC-TM and 847A showed strong affinities for the postfusion-specific, site I-directed non-NAb, ADI-14359, whereas negligible binding was observed for both DS-Cav1 and sc9-10 DS-Cav1 designs regardless of the purification method used. For most NAbs targeting sites II - V, the four designs showed similar binding profiles, with relatively low affinity noted for Nickel/SEC-purified 847A-His_6 and DS-Cav1-His_6. For NAb MPE8[63], which cross-neutralizes RSV and hMPV by targeting site III, 847A-His_6 showed the lowest affinity among the five constructs. NAbs AM14 and ADI-19425[32,48] were included to probe the two interface epitopes. For AM14 (the IV-V interface), sc9-10 DS-Cav1 showed the highest binding affinity, whereas DS-Cav1-His_6 defined the lowest with a fold difference of 14–110 in EC_{50}, consistent with the open/dissociated trimers observed in the nsEM analysis (Fig. 1a, right). For ADI-19425 (the III-IV interface), sc9-10 DS-Cav1 exhibited low binding affinity, likely due to the interprotomer disulfide bond altering the III-IV interface[44]. All five RSV-F samples were then subjected to biolayer interferometry (BLI) using the same antibody panel. The peak binding signals and equilibrium dissociation constant (K_D) were determined to assess their antigenic properties (Fig. 1f and Fig. S1g). The BLI signals of these RSV-F constructs binding to the postfusion-specific ADI-14359 were consistent with the ELISA data (Fig. 1e). For sc9-10 DS-Cav1, D25 purification resulted in consistently higher NAb binding signals than Nickel purification (Fig. 1f).

The two DS-Cav1 constructs were used to assess the effect of the P27 peptide, C-terminal trimerization motif, and expression system on the resulting RSV-F protein. The p27 peptide, which hinders F trimerization if not properly removed[33], was deleted from DS-Cav1[43] to generate a DS-Cav1Δp27 construct with a single cleavage site. D25-purified DS-Cav1Δp27 showed similar in vitro properties to Nickel-purified DS-Cav1-His_6 in the SEC, DSC, and nsEM analyses (Fig. S1i) but with markedly improved antigenic profiles (Fig. S1j). Removal of the C-terminal foldon motif resulted in the dissociation of DS-Cav1Δp27 and sc9-10 DS-Cav1 trimers into monomers, with small aggregate and trimer peaks observed for the latter, regardless of the antibody columns used for purification (Fig. S1k). In terms of expression system, a differential effect of ExpiCHO *vs.* HEK293F expression was observed for the two DS-Cav1 constructs after Nickel purification (Fig. S1l). For DS-Cav1Δp27-His_6, ExpiCHO produced a lower aggregate peak in the SEC profile than HEK293F. In contrast, sc9-10 DS-Cav1-His_6 showed no significant difference in SEC using either expression system. Consistently, the nsEM analysis indicated higher structural quality for DS-Cav1Δp27-His_6 expressed in ExpiCHO cells, whereas sc9-10 DS-Cav1-His_6 always contained ~100% prefusion-closed trimers, regardless of the cell lines used for expression.

Our results revealed unique properties associated with four previous RSV-F designs, which were used as controls. Overall, sc9-10 DS-Cav1 was the best performer, with ~100% prefusion closed trimers and well-preserved NAb epitopes, whereas two of the other RSV-F constructs (SC-TM-His_6 and 847A-His_6) expressed a detectable level of postfusion F. Our results did not always match previous data for these designs, which might be caused by differences in construct design, expression, purification, or sample handling; however, all of our experiments were conducted using the same methods throughout the study with some of the key factors examined in detail. This comparative analysis informed our design of a new generation of prefusion RSV-F.

Design of uncleaved prefusion-closed (UFC) RSV-F trimers with minimum mutations

Sc9-10 DS-Cav1[44] produces prefusion-closed trimers with high yield and purity but at the cost of introducing a large set of mutations and an interprotomer disulfide bond that alters a major NAb epitope. Here, we hypothesized that an uncleaved prefusion-closed (UFC) trimer could be designed for RSV-F involving a smaller set of mutations. We first

https://doi.org/10.1038/s41467-024-54287-x

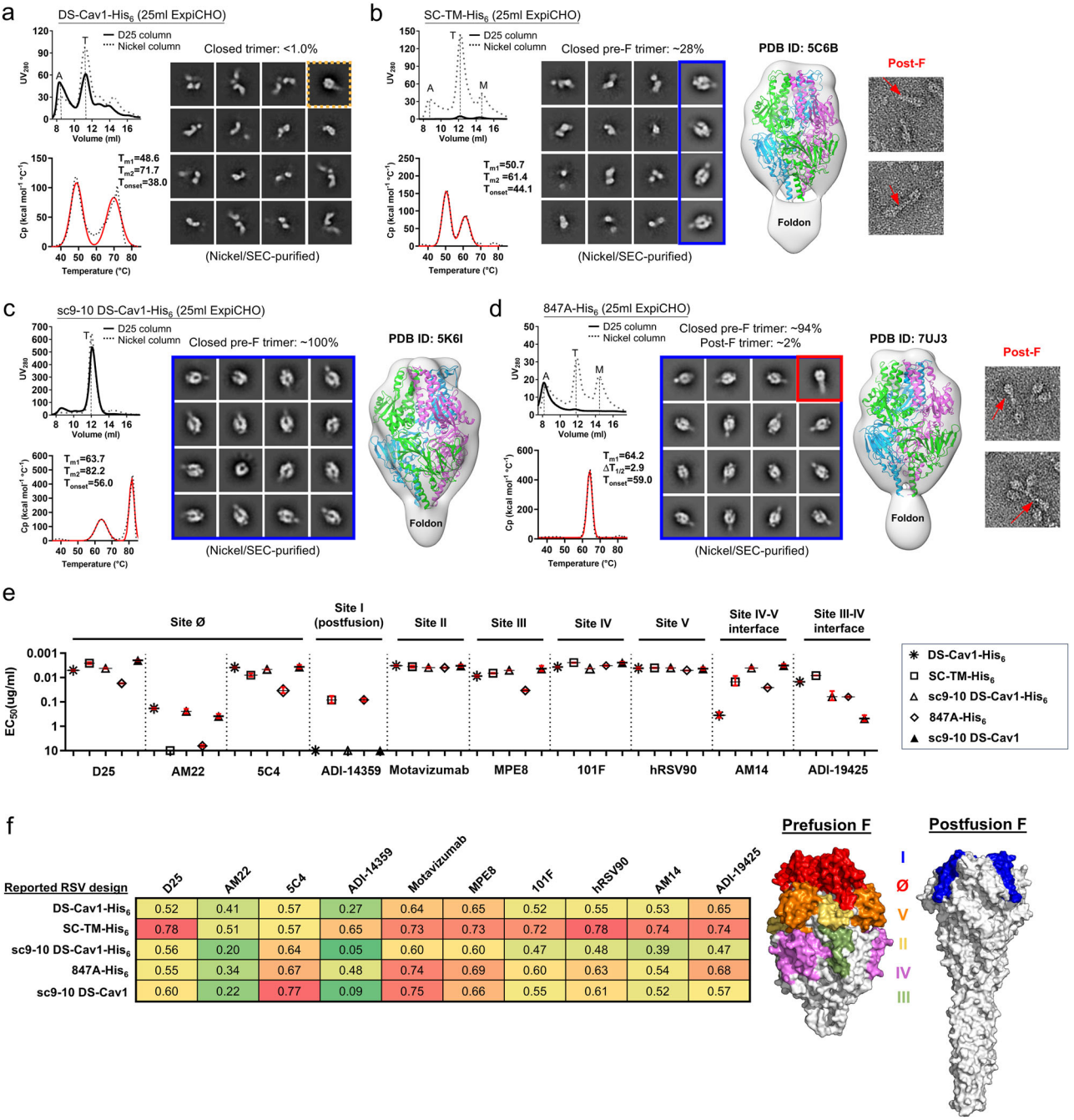

Reported RSV design	D25	AM22	5C4	ADI-14359	Motavizumab	MPE8	101F	hRSV90	AM14	ADI-19425
DS-Cav1-His_6	0.52	0.41	0.57	0.27	0.64	0.65	0.52	0.55	0.53	0.65
SC-TM-His_6	0.78	0.51	0.57	0.65	0.73	0.73	0.72	0.78	0.74	0.74
sc9-10 DS-Cav1-His_6	0.56	0.20	0.64	0.05	0.60	0.60	0.47	0.48	0.39	0.47
847A-His_6	0.55	0.34	0.67	0.48	0.74	0.69	0.60	0.63	0.54	0.68
sc9-10 DS-Cav1	0.60	0.22	0.77	0.09	0.75	0.66	0.55	0.61	0.52	0.57

Fig. 1 | Comparative in vitro characterization of previously reported RSV-F designs. Size exclusion chromatography (SEC) profile (left top), differential scanning calorimetry (DSC) profile (left bottom), representative 2D classification images (middle, or right when no 3D models are shown), and 3D reconstruction from the nsEM analysis (right) for (**a**) DS-Cav1, (**b**) SC-TM, (**c**) Sc9-10 DS-Cav1, and (**d**) 847A. All constructs contain a foldon trimerization motif with or without a C-terminal His_6 tag, indicated in the construct name with a suffix (-His_6). A total of 8 constructs were transiently expressed in 25 ml of ExpiCHO cells and purified using a Nickel column or a D25 antibody column. Major SEC peaks, such as aggregation (A), trimer (T), and monomer (M), are marked on the profile. The SEC profiles after Nickel and D25 antibody purification are shown as dotted and solid lines, respectively. For the 2D classification analysis, prefusion-closed trimers are circled in a blue line box, and closed trimers in the postfusion and non-prefusion states are circled in a red line box and a dotted orange line box, respectively. For SC-TM-His_6 and 847A-His_6, two micrographs are enlarged to show shapes characteristic of the postfusion F. Prefusion RSV-F trimer structures (PDB ID: 5C6B, 5K6I, and 7UJ3) are used for structural fitting into the nsEM densities. **e** ELISA-derived EC_{50} (μg/ml) values of five RSV-F trimers binding to 10 antibodies that target six antigenic sites and two interface epitopes, which are labeled on the plots. If absorbance at 450 nm is less than 0.5 at the starting and highest concentration (10 μg/ml), then the antigen has negligible binding to the tested antibody, and the EC_{50} value is set to 10 μg/ml. Error bars represent the difference between duplicates at each concentration tested for each sample. **f** Biolayer interferometry (BLI) antigenic profiles of five RSV-F trimers binding to the same antibodies. Sensorgrams were obtained from an Octet RED96 instrument using an antigen titration series of six concentrations (starting at 600 nM followed by 2-fold dilutions) and are shown in Fig. S1g. Peak values at the highest concentration are shown in a matrix, in which cells are colored in green (weak binding) to red (strong binding) (left). In (e) and (f), the four His-tagged RSV-F trimers were purified using a Nickel column, whereas sc9-10 DS-Cav1 was purified using a D25 antibody column. **g** Footprints of six antigenic sites colored on the surface representation of prefusion (PDB ID: 4JHW) and postfusion (PDB ID: 3RRR) RSV-F trimers (right).

derived a base construct, termed UFC_{R1}, which contains the same F_2-F_1 connecting region as in sc9-10 DS-Cav1[44], an intra-F_1 disulfide bond (S155C-S290C), and S215P and E92D mutations (Fig. S2a and Table S1b). A foldon motif was attached to the F_1 C-terminus in UFC_{R1} and all its derivatives. We further hypothesized that a second proline mutation (V185P, or named P2) in the $HR1_N$-equivalent β3-β4 hairpin[71] might destabilize the postfusion state, resulting in a UFC_{R1}-P2 construct. Lastly, we hypothesized that the acidic patch (^{486}DEFD^{489}) atop the coiled-coil F_1 stalk is a major cause of RSV-F metastability, and a hydrogen bond (D486N/E487Q, or NQ) mutation or a hydrophobic (D486L/E487L, or L2) mutation might effectively maintain prefusion RSV-F in a closed trimer conformation.

Four constructs, UFC_{R1}, UFC_{R1}-P2, UFC_{R1}-P2-NQ, and UFC_{R1}-P2-L2, were characterized. Based on the overall more favorable antigenic properties of sc9-10 DS-Cav1 after D25 purification (Fig. 1e-f), all constructs were purified by a D25 affinity column following ExpiCHO expression. UFC_{R1} produced a similar SEC profile to sc9-10 DS-Cav1 with high trimer yield and purity (Fig. 2a, left top) but was less thermostable with lower T_{m1} (57.1 °C) and T_{m2} (72.4 °C) values (Fig. 2a, left bottom). In the nsEM analysis, only ~4% of UFC_{R1} represented prefusion-closed trimers in 2D classes, which were used for 3D reconstruction and modeling (Fig. 2a, right). UFC_{R1}-P2 generated a similar SEC profile with slightly reduced thermostability (1.3 °C and 5.7 °C lower for T_{m1} and T_{m2}, respectively) compared with UFC_{R1} (Fig. 2b, left). In addition, UFC_{R1}-P2 contained a similar fraction (~4%) of prefusion-closed trimers in the nsEM analysis, although image quality was insufficient for 3D modeling (Fig. 2b, right). UFC_{R1}-P2-NQ and UFC_{R1}-P2-L2 represented two designs to avoid the interprotomer disulfide bond (A149C-Y458C) by altering the acidic patch. In wildtype RSV-F, this acidic patch creates "repulsive" charge-charge interactions around the trimer axis, thus destabilizing the closed trimer. For UFC_{R1}-P2-NQ, the NQ mutation had little effect on trimer expression, generating a similar SEC profile to UFC_{R1} and UFC_{R1}-P2 (Fig. 2c, left top). In the DSC analysis, the melting points remained comparable, but T_{onset} increased to 50 °C (Fig. 2c, left bottom), suggesting a delayed denaturing step during heating. Notably, the nsEM analysis revealed a significantly higher ratio (73%) of prefusion-closed trimers, which allowed reliable 3D reconstruction and density fitting using a prefusion RSV-F structure (PDB ID: 4JHW) (Fig. 2c, right)[42]. The effects of hydrophobic mutations at the acidic patch were examined using the UFC_{R1}-P2-L2 construct. Overall, UFC_{R1}-P2-L2 demonstrated a similar expression profile to other UFC_{R1} variants (Fig. 2d, left top). In terms of thermostability, UFC_{R1}-P2-L2 had a further increase in T_{onset} (52.1 °C) compared with UFC_{R1}-P2-NQ (Fig. 2d, left bottom). In the nsEM analysis, UFC_{R1}-P2-L2 produced a slightly higher ratio of prefusion-closed trimers than UFC_{R1}-P2-NQ, ~76% *vs.* ~73%, respectively (Fig. 2d, right). Based on these results, we combined a prefusion-specific NAb, D25, and a postfusion-specific non-NAb, ADI-14359, with nsEM to probe UFC_{R1}-P2-NQ and UFC_{R1}-P2-L2. In both cases, we observed D25 Fab-bound trimers, in addition to unbound D25 Fabs, unbound prefusion F monomers, and D25 Fab-bound prefusion F monomers (Fig. 2e, left; Fig. S2b, left). Importantly, both RSV-F trimers remained prefusion in the presence of ADI-14359, confirmed by the 2D classification and 3D reconstruction (Fig. 2e, right; Fig. S2b, right). Lastly, the reducing SDS-PAGE analysis of crosslinked samples demonstrated consistent trimer bands on the gel, suggesting high homogeneity of the UFC_{R1} series (Fig. S2c).

Antigenicity of the four UFC_{R1} constructs was evaluated by ELISA and BLI using the 10-antibody panel. All four constructs showed high affinities for prefusion-specific, site Ø-targeting NAbs except AM22. In the ELISA, UFC_{R1}-P2-NQ exhibited stronger binding to D25 than UFC_{R1}-P2-L2, with EC_{50} values of 0.003 and 0.006 μg/ml, respectively (Fig. 2f, Fig. S2d). In BLI, UFC_{R1}-P2-L2 showed a slightly higher D25-binding signal than UFC_{R1}-P2-NQ (Fig. 2g, Fig. S2e). Notably, a detectable, albeit low, signal was observed for UFC_{R1}-P2-L2 binding to the postfusion-specific site I-directed non-NAb, ADI-14359[48], in both the ELISA and BLI. This unexpected result highlights the intricate balance between trimer stabilization and postfusion transition for mutations to the buried acidic patch. Because ADI-14359-bound UFC_{R1}-P2-L2 trimers were not identified in any EM micrographs, a plausible explanation is that strong hydrophobic interactions introduced by the L2 mutation can cause conformational breathing that would transiently expose site I but could not escalate to an irreversible transition to the postfusion state. All four UFC_{R1} constructs showed high affinities for NAb ADI-19425[48] (EC_{50} = 0.007–0.009 μg/ml), confirming that removal of the interprotomer disulfide bond can restore the III-IV interface epitope.

A His-tagged UFC_{R1}-P2-NQ was used to assess the effect of expression and purification on the newly designed RSV-F. Following ExpiCHO expression, Nickel-purified UFC_{R1}-P2-NQ-His_6 was analyzed by SEC and tested for antibody binding by ELISA (Fig. S2g). Nearly identical EC_{50} values were obtained for D25- and Nickel-purified samples (with greater yield noted for the latter), suggesting a negligible effect of purification methods on antigenicity for this construct. Although HEK293F expression rendered a similar SEC profile to ExpiCHO expression, only ~60% of UFC_{R1}-P2-NQ-His_6 trimers were closed in the nsEM analysis after Nickel/SEC purification (Fig. S2h). These results aligned well with the findings for the two DS-Cav1 variants (Fig. S1l).

Crystallographic characterization of UFC_{R1}-series RSV-F trimers

Although low-resolution nsEM demonstrated that the NQ and L2 mutations substantially increased the ratio of prefusion-closed trimers, x-ray crystallography can provide atomic details of the altered interactions at the acidic patch. To this end, five crystal structures were obtained to validate RSV-F designs in a stepwise manner (Tables S1b and S2). The crystal structure of a ligand-free UFC_{R1} was determined at a resolution of 2.26 Å. The UFC_{R1} protomer showed root-mean-square deviations (RMSDs) of Cα atoms (Cα-RMSD) at 0.86 and 0.67 Å relative to DS-Cav1 (PDB ID: 4MMU)[43] and sc9-10 DS-Cav1 (PDB ID: 5K6I)[44], respectively, whereas a larger Cα-RMSD value of 1.13 Å was determined between DS-Cav1 and sc9-10 DS-Cav1 (Fig. S3). Notably, although the majority of UFC_{R1} adopted various open trimer forms in solution (Fig. 2a, middle), UFC_{R1} was seen in a fully closed trimer form in the crystal structure, suggesting that even a small percentage of closed trimers can crystallize (Fig. 3a). We also created a variant of UFC_{R1}, with a 5GS flexible linker between RSV-F and a different trimerization motif (PDB ID: 1TD0), which was used in our previous studies[68,69,79]. Indeed, a crystal structure at 2.28 Å resolution was obtained for UFC_{R1}(1TD0), showing a Cα-RMSD of 0.50 Å relative to UFC_{R1} at the protomer level (Fig. 3a, right). Structural superimposition revealed largely similar backbone conformations (Cα-RMSD: 2.24 Å) for the loop connecting F_2-S99 and F_1-A149 (Fig. 3a, left), which would be buried within a prefusion-closed trimer. Next, we obtained a 2.70 Å-resolution crystal structure for UFC_{R1}-P2-NQ, which largely resembled the UFC_{R1} structure with a Cα-RMSD of 0.53 Å at the protomer level (Fig. 3b, right). The V185P mutation disrupted a backbone hydrogen bond near the tip of the β3-β4 hairpin in the prefusion F (Fig. 3b, left) and would likely cause a "kink" in the extended α5 helix in the postfusion state[80]. Similar proline mutations in $HR1_N$ or $HR1_N$-equivalent regions have been reported for prefusion-stabilized designs of HIV-1 Env[70,71,81] and EBOV GP[69,82]. The D486N/E487Q mutation replaced the repulsive charge-charge interaction with a hydrogen bond across the protomer interface (Fig. 3b, bottom), thus helping maintain the prefusion-closed trimer conformation. We also obtained a 2.30 Å-resolution crystal structure for UFC_{R1}-L2 (Fig. 3c, left). UFC_{R1}-L2 and UFC_{R1} shared high structural similarity, with a protomer Cα-RMSD of 0.50 Å. In the UFC_{R1}-L2 structure, two L486 residues of adjacent protomers form a hydrophobic contact across the interface, with Cγ-Cγ and Cδ-Cδ distances of 5.4 and 3.9 Å, respectively (Fig. 3c, right). By

https://doi.org/10.1038/s41467-024-54287-x

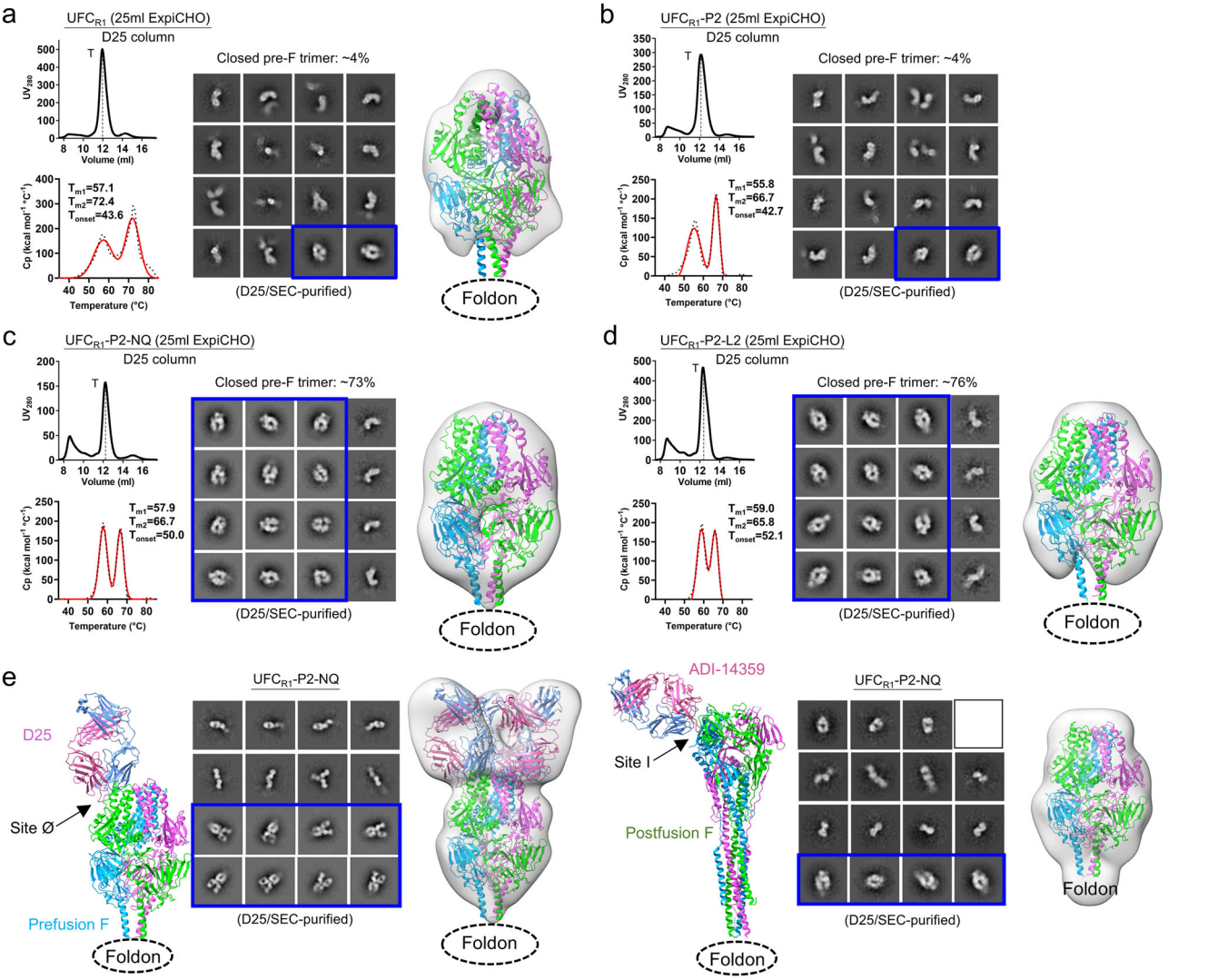

g

RSV UFC$_{R1}$ series	D25	AM22	5C4	ADI-14359	Motavizumab	MPE8	101F	hRSV90	AM14	ADI-19425
UFC$_{R1}$	0.65	0.22	0.70	0.08	0.67	0.71	0.54	0.56	0.56	0.71
UFC$_{R1}$-P2	0.61	0.23	0.70	0.14	0.63	0.66	0.52	0.53	0.51	0.68
UFC$_{R1}$-P2-NQ	0.74	0.25	0.76	0.14	0.84	0.74	0.63	0.65	0.59	0.81
UFC$_{R1}$-P2-L2	0.77	0.19	0.76	0.22	0.74	0.69	0.62	0.62	0.59	0.70

Fig. 2 | Design and in vitro characterization of RSV-F UFC$_{R1}$ series. SEC profile (left top), DSC profile (left bottom), representative 2D classification images (middle, or right when no 3D models are shown), and 3D reconstruction from nsEM analysis (right) for (**a**) UFC$_{R1}$, (**b**) UFC$_{R1}$-P2, (**c**) UFC$_{R1}$-P2-NQ, and (**d**) UFC$_{R1}$-P2-L2. All UFC$_{R1}$ constructs were transiently expressed in 25 ml of ExpiCHO cells and purified using a D25 antibody column. The trimer (T) peak is marked on the profile. **e** The nsEM analysis of UFC$_{R1}$-P2-NQ in the presence of prefusion-specific antibody D25 (left panel) or postfusion-specific antibody ADI-14359 (right panel). Each panel shows the ribbon model of the RSV-F/antibody complex (left), representative 2D classification images (middle), and 3D reconstruction (right). The 2D classes corresponding to prefusion-closed trimers (either ligand-free or antibody-bound) are circled in blue, and a prefusion RSV-F trimer (PDB ID: 4JHW) was used for structural fitting into the nsEM densities. **f** ELISA-derived EC$_{50}$ (μg/ml) values of four UFC$_{R1}$ constructs binding to 10 antibodies, as in Fig. 1e. **g** BLI-derived antigenic profiles of four UFC$_{R1}$ constructs binding to 10 antibodies. Sensorgrams were obtained using the same protocol as in Fig. 1f and are shown in Fig. S2e. The matrix of peak values at the highest antigen concentration is shown, as in Fig. 1f.

https://doi.org/10.1038/s41467-024-54287-x

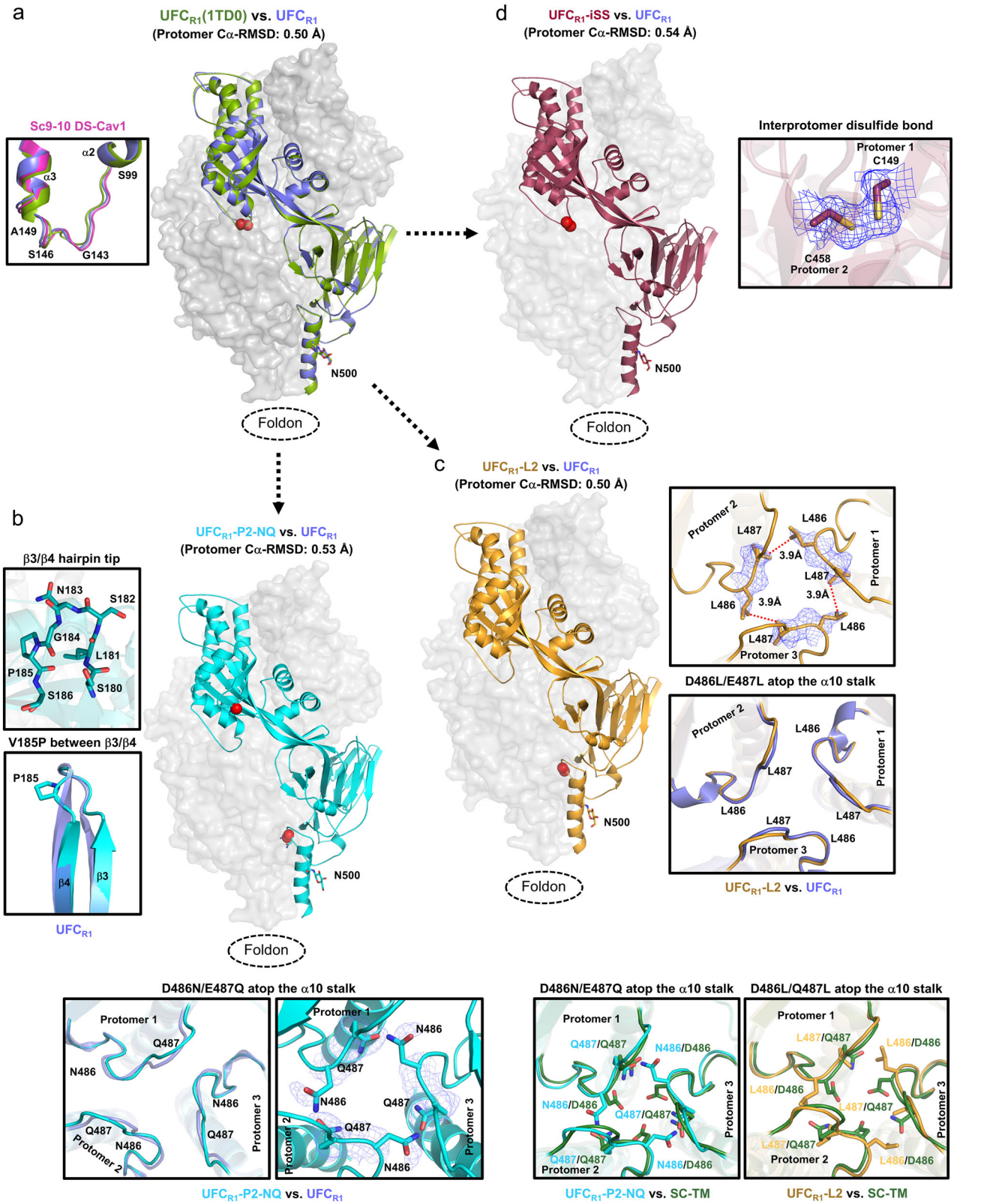

comparison, residues 486 and 487 do not interact in the crystal structures of SC-TM[33] or 847A[45], which contain E487Q and D486S mutations, respectively (Fig. 3c, bottom). Lastly, we examined whether adding the interprotomer disulfide bond (A149C-Y458C, or iSS) to UFC_{R1} would create a "simplified" version of sc9-10 DS-Cav1. A 2.30 Å-resolution crystal structure was obtained for this UFC_{R1}-iSS construct (Fig. 3d, left). As expected, UFC_{R1}-iSS structurally resembled both UFC_{R1} and sc9-10 DS-Cav1, with protomer Cα-RMSDs of 0.54 and 0.61 Å, respectively. The interprotomer disulfide bond adopted a nearly identical geometry to that in sc9-10 DS-Cav1[44] (Fig. 3d, right). Altogether, our crystallographic analyses provided detailed structural information supporting the UFC_{R1}-series design principles.

Fig. 3 | Crystallographic analysis of RSV-F UFC_{R1} series and variants. a Crystal structures of UFC_{R1} and UFC_{R1}(1TD0) (2.26 and 2.28 Å) are superimposed and shown as green and blue ribbon models, respectively, within the gray trimer surface. The F_2-F_1 linkage is shown for UFC_{R1} and UFC_{R1}(1TD0) relative to sc9-10 DS-Cav1 (pink) in the left inset. **b** The crystal structure of UFC_{R1}-P2-NQ (2.70 Å) is shown as a cyan ribbon model within the gray trimer surface. The atomic model of the β3/β4 hairpin tip and a close-up view of the V185P mutation between β3 and β4 are shown in the left insets, and the backbone and side chains of acidic patch mutations in UFC_{R1}-P2-NQ (D486N-E487Q) are compared with UFC_{R1} in the bottom insets. **c** The crystal structure of UFC_{R1}-L2 (2.30 Å) is shown as a gold ribbon model within the gray trimer surface. The backbone and side chains of acidic patch mutations in UFC_{R1}-L2 (D486L-E487L) are compared with UFC_{R1} in the right insets, and structural details of this region in UFC_{R1}-P2-NQ and UFC_{R1}-L2 are compared with SC-TM in the bottom insets. **d** The crystal structure of UFC_{R1}-iSS (2.3 Å) is shown as a red ribbon model within the gray trimer surface. A close-up view of the interprotomer disulfide bond (A149C-Y458C) within the density is shown in the right inset. All electron densities (2Fo-Fc) are shown at 1σ in blue mesh. Red spheres mark the amino acid difference between the two superimposed UFC_{R1} structures, which are shown as ribbon models.

Design and characterization of UFC_{R2}-series RSV-F constructs

To investigate whether additional mutations can improve the ratio of prefusion-closed trimers, we created a second base construct, termed UFC_{R2}, by adding two mutations (S46G and K465Q) to UFC_{R1}. A total of four constructs, UFC_{R2}, UFC_{R2}-P2, UFC_{R2}-P2-NQ, and UFC_{R2}-P2-L2 (Fig. S4a and Table S1c), were evaluated using a similar strategy to UFC_{R1} (Fig. 4). For UFC_{R2}, the SEC profile contained a shifted trimer peak (at ~11.1 ml for UFC_{R2} *vs.* ~ 11.9 ml for UFC_{R1}) and a visible monomer peak (Fig. 4a, left top). Although UFC_{R2} appeared to be more thermostable than UFC_{R1}, indicated by higher T_{m2} (75.9 °C *vs.* 72.4 °C) and T_{onset} (51.4 °C *vs.* 43.6 °C) values (Fig. 4a, left bottom), no 2D classes representing prefusion-closed trimers were found by nsEM (Fig. 4a, right). In fact, D25-purified UFC_{R2} exhibited a tendency to dissociate into monomers. UFC_{R2}-P2 behaved similarly to UFC_{R2} with less monomer content, indicated by both SEC (Fig. 4b, left top) and nsEM (Fig. 4b, right), although its thermostability was slightly reduced, indicated by DSC (T_{m1} = 56.2 °C, T_{m2} = 69.9 °C, and T_{onset} = 48.3 °C) (Fig. 4b, left bottom). Incorporation of the NQ or L2 mutation generated a similar effect on the resulting UFC_{R2}-P2-NQ and UFC_{R2}-P2-L2 constructs, as it did on their UFC_{R1} counterparts (Fig. 4c, d). Briefly, both mutations reduced the SEC peak corresponding to dissociated monomers, with UFC_{R2}-P2-L2 showing the highest trimer purity (Fig. 4c, d, left top). Similarly, these two mutations also improved RSV-F thermostability, with L2 slightly outperforming NQ in terms of T_{m1} (59.5 °C *vs.* 58.5 °C), which was ~2–3 °C higher than those of UFC_{R2} and UFC_{R2}-P2 (Figs. 4c and 4d, left bottom). However, nsEM revealed a significant difference in the ratio of prefusion-closed trimers between UFC_{R2}-P2-NQ and -L2 following D25 and SEC purification, ~6% and ~28%, respectively (Fig. 4c, d, middle). Nonetheless, fitting a prefusion RSV-F structure (PDB ID: 4JHW)[43] into the nsEM densities (Fig. 4c, d, right) confirmed that both constructs produced prefusion-closed trimers. In reducing SDS-PAGE, crosslinked UFC_{R2} and UFC_{R2}-P2 showed higher bands on the gel compared with UFC_{R2}-P2-NQ and UFC_{R2}-P2-L2 (Fig. S4b), indicating an open form of the trimer structure. Therefore, two distant, seemingly unrelated mutations, S46G in β2 and K465Q in β22[44], appeared to significantly reduce the ratio of prefusion-closed RSV-F trimers.

Although extensive screening of the UFC_{R2} constructs did not result in diffraction-quality crystals, the interprotomer disulfide bond (A149C-Y458C, iSS) stabilized the UFC_{R2} constructs and led to three crystal structures (Tables S1c, S3). UFC_{R2}-iSS yielded Cα-RMSDs of 1.09 and 0.55 Å relative to DS-Cav1 and sc9-10 DS-Cav1, respectively (Fig. S4c). It was unsurprising that UFC_{R2}-iSS was structurally more similar to sc9-10 DS-Cav1 because two additional mutations (S46G and K465Q) from sc9-10 DS-Cav1 were included in the UFC_{R2} construct. Structural superposition revealed nearly identical UFC_{R1}-iSS and UFC_{R2}-iSS backbones with a protomer Cα-RMSD of 0.48 Å (Fig. 4e, left), indicating that the S46G and K465Q mutations had little impact on the prefusion RSV-F structure. Compared with UFC_{R2}-iSS, the NQ mutation resulted in the backbone of the acidic patch moving slightly outward toward each protomer, with a local Cα-RMSD of 1.40 Å, to make room for the hydrogen bond between N486 and Q487 across the protomer interface in UFC_{R2}-iSS-NQ (Fig. 4e, middle and left inset). Lastly, a UFC_{R2}-iSS-P2-NQ construct was created and assessed by the SEC, DSC, and nsEM analyses after D25 purification (Fig. S4d). In SEC, UFC_{R2}-iSS-P2-NQ showed higher trimer yield but with a minor aggregate peak compared with UFC_{R2}-P2-NQ and UFC_{R2}-P2-L2. As expected, UFC_{R2}-iSS-P2-NQ exhibited greater thermostability than UFC_{R2}-P2-NQ and UFC_{R2}-P2-L2 due to the trimer-locking disulfide bond. The nsEM analysis revealed 84.6% prefusion-closed trimers for this construct. In the crystal structure, UFC_{R2}-iSS-P2-NQ showed nearly identical hydrogen bonding patterns to UFC_{R2}-iSS-NQ and an unchanged β4 backbone despite the V185P (or P2) mutation (Fig. 4e, right and left inset). These results suggest that the S46G/K465Q mutation makes the UFC_{R2} backbone more flexible and potentially more amenable to global structural changes caused by mutations.

Antigenicity of five UFC_{R2}-series constructs, including UFC_{R2}, UFC_{R2}-P2, UFC_{R2}-P2-NQ, UFC_{R2}-P2-L2, and UFC_{R2}-iSS-P2-NQ, was evaluated by ELISA (Fig. 4f, Fig. S4e) and BLI (Fig. 4g, Fig. S4f) using the 10-antibody panel. Overall, the UFC_{R2} series generated similar antigenic profiles to their UFC_{R1} counterparts. In the ELISA, UFC_{R2}-P2-L2 showed low levels of ADI-14359 binding (EC_{50} = 0.32 μg/ml) as did UFC_{R1}-P2-L2, confirming the conformational breathing effect of the L2 mutation. In addition, UFC_{R2} and UFC_{R2}-P2 showed lower affinities for ADI-19425 than UFC_{R2}-P2-NQ and -L2, with a ~ 12-fold difference in EC_{50}, consistent with the finding that UFC_{R2} and UFC_{R2}-P2 did not produce any prefusion-closed trimers in nsEM and thus bound less favorably to NAbs targeting the III-IV interface. The iSS mutation (A149C-Y458C) adversely affected UFC_{R2}-iSS-P2-NQ binding to ADI-19425, as this interprotomer disulfide bond might alter the structure of the III-IV interface required for ADI-19425 recognition. To verify this effect, we tested the binding of UFC_{R2}-iSS-P2-NQ, along with UFC_{R1}-P2-NQ and two DS-Cav1 variants, to VHH-L66-His_6, a nanobody that exploits a cavity bordered by sites II and IV of two protomers in a prefusion-closed trimer[83,84] (Fig. S4g). Indeed, the two RSV-F constructs that contain the interprotomer disulfide bond, UFC_{R2}-iSS-P2-NQ and sc9-10 DS-Cav1[44], bound less favorably to VHH-L66-His_6, as they did to ADI-19425 (Figs. 1e, 4f). By comparison, UFC_{R1}-P2-NQ showed saturated binding signals with 10.8-times greater affinity than sc9-10 DS-Cav1[44].

Alternative mutations to the $HR1_N$-equivalent β3-β4 hairpin revealed by the UFC_{R3} series

In our previous studies, the $HR1_N$ bend, or $HR1_N$-equivalent region, was identified as the major contributor to the metastability of HIV-1 Env[70,71] and EBOV GP[69,82]. Notably, the $HR1_N$-equivalent region in prefusion RSV-F adopts a hairpin formed by β3 and β4, compared with a 21-aa unstructured loop in HIV-1 Env and an 8-aa turn (termed $HR1_C$) between two HR1 helices in EBOV GP. In addition to the proline mutation (V185P), other mutations may be designed to target the β3-β4 hairpin. To this end, we created a third type of construct, termed UFC_{R3}, which contains a longer linker $(GS)_4$ between F_2-T103 and F_1-A147, an intra-F_1 disulfide bond (S155C-S290C), the S215P mutation, and a second intra-F_1 disulfide bond (A177C-T189C) specifically designed to lock β3 and β4 in the prefusion hairpin structure and prevent the pre- to postfusion transition (Fig. S5a and Table S1d). We structurally characterized UFC_{R3} and its two variants using x-ray crystallography (Table S4). A crystal structure was obtained for UFC_{R3} at a resolution of 2.69 Å, which showed a Cα-RMSD of 0.74 Å relative to

https://doi.org/10.1038/s41467-024-54287-x

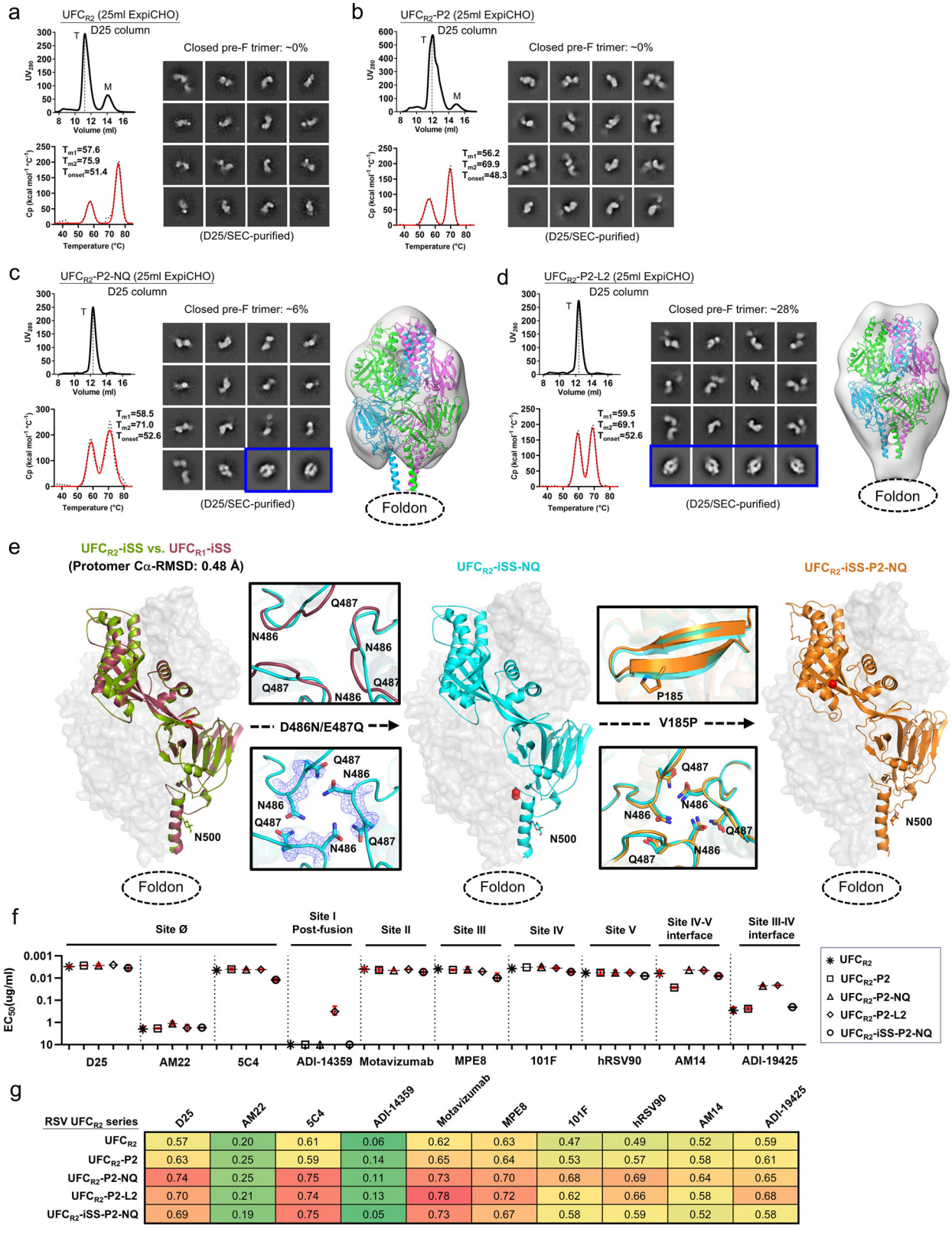

g

RSV UFC$_{R2}$ series	D25	AM22	5C4	ADI-14359	Motavizumab	MPE8	101F	hRSV90	AM14	ADI-19425
UFC$_{R2}$	0.57	0.20	0.61	0.06	0.62	0.63	0.47	0.49	0.52	0.59
UFC$_{R2}$-P2	0.63	0.25	0.59	0.14	0.65	0.64	0.53	0.57	0.58	0.61
UFC$_{R2}$-P2-NQ	0.74	0.25	0.75	0.11	0.73	0.70	0.68	0.69	0.64	0.65
UFC$_{R2}$-P2-L2	0.70	0.21	0.74	0.13	0.78	0.72	0.62	0.66	0.58	0.68
UFC$_{R2}$-iSS-P2-NQ	0.69	0.19	0.75	0.05	0.73	0.67	0.58	0.59	0.52	0.58

sc9-10 DS-Cav1 at the protomer level (Fig. S5b, left). In the first variant, the S46G/E86D/K465Q triple mutation was added into UFC$_{R3}$, resulting in a 2.31 Å-resolution structure for UFC$_{R3}$-GDQ, with a protomer Cα-RMSD of 0.76 Å relative to sc9-10 DS-Cav1 (Fig. S5b, middle). In the second variant, E86D was added to UFC$_{R3}$ with viral capsid protein SHP (PDB ID: 1TD0) replacing the foldon as the trimerization motif, resulting in a 3.20 Å-resolution structure for UFC$_{R3}$-D(1TD0), with a protomer Cα-RMSD of 0.89 Å relative to sc9-10 DS-Cav1 (Fig. S5b, right). In all three structures, the extended F_2-F_1 loop formed a 4-residue protrusion in the middle of the loop and was found buried within the cavity of the closed trimer (Fig. S5b, right, top inset), whereas β3 and β4 exhibited slightly twisted backbones that facilitated disulfide bond formation (Fig. S5b, right, bottom inset). Crystallographic analyses of these UFC$_{R3}$ variants revealed that prefusion

Fig. 4 | Design, in vitro characterization, and crystallographic analysis of RSV-F UFC_{R2} series. SEC profile (left top), DSC profile (left bottom), representative 2D classification images (middle, or right when no 3D models are shown), and 3D reconstruction from nsEM analysis (right) for (**a**) UFC_{R2}, (**b**) UFC_{R2}-P2, (**c**) UFC_{R2}-P2-NQ, and **d** UFC_{R2}-P2-L2. All UFC_{R2} constructs were transiently expressed in 25 ml of ExpiCHO cells and purified using a D25 antibody column. The trimer (T) peak is marked on the profile. The 2D classification images corresponding to prefusion-closed trimers are circled in blue, and a prefusion RSV-F trimer (PDB ID: 4JHW) is used for structural fitting into the nsEM densities. **e** Crystallographic analysis of three UFC_{R2}-derived constructs. Left: Crystal structures of UFC_{R2}-iSS and UFC_{R1}-iSS (2.83 and 2.30 Å) are superimposed and shown as green and red ribbon models, respectively, within the gray trimer surface. Middle: The crystal structure of UFC_{R2}-iSS-NQ (2.30 Å) is shown as a cyan ribbon model within the gray trimer surface. The backbone and side chains of acidic patch mutations in UFC_{R3}-iSS-NQ (D486N-E487Q) are compared with UFC_{R2}-iSS in the insets to the left of the protomer/surface model. Right: The crystal structure of UFC_{R2}-iSS-P2-NQ (2.30 Å) is shown as a gold ribbon model within the gray trimer surface. Details of the V185P mutation and acidic patch are shown in the insets to the left of the protomer/surface model. **f** ELISA-derived EC_{50} (μg/ml) values of five UFC_{R2} constructs binding to 10 antibodies, as in Fig. 1e. **g** BLI-derived antigenic profiles of five UFC_{R2} constructs binding to 10 antibodies. Sensorgrams were obtained using the same protocol as in Fig. 1f and are shown in Fig. S4e. The matrix of peak values at the highest antigen concentration is shown, as in Fig. 1f.

RSV-F can tolerate various mutations in the $HR1_N$-eqivalent β3-β4 hairpin and F_2-F_1 linkage, in addition to different trimerization motifs.

Design and in vitro characterization of prefusion hMPV-F constructs

Multiple designs have been proposed to stabilize prefusion hMPV-F[35,60–62] (Fig. S6a, Table S5a). In the cleaved DS-CavEs2, Hsieh et al. introduced a disulfide bond (T365C-V463C) between β14 and α10 to stabilize this membrane-proximal region, which, however, could also destabilize the C-terminal stalk essential to F trimerization[61]. As a result, the crystallographic analysis revealed that DS-CavEs2 is a pre-fusion monomer[61]. Kwong and colleagues evaluated various disulfide bonds, proline mutations, and cleavage site linkers[60,62], arriving at a construct containing a short F_2-F_1 linker and three disulfide bonds[60]. In their construct design, the D454C-V458C mutation was initially introduced as an interprotomer disulfide bond, but cryo-EM revealed the formation of an intra-F_1 disulfide bond that drastically altered the local structure around the trimer base[60]. Here, we followed a minimalist approach, akin to what we used for RSV, to rationally design UFC trimers for hMPV-F. To this end, we developed a base construct, termed UFC_{M1}, which places a G6 linker between the shortened F_2 C-terminus (F_2-E92) and fusion peptide (F_1-103), in addition to A185P, E80D, and disulfide bond (T127C-N153C) mutations, as well as a C-terminal His_6 tag (Fig. S6b, Table S5b). We then hypothesized that a second proline mutation (V155P, or P2) in the $HR1_N$-equivalent region[71] can destabilize the postfusion state, yielding a UFC_{M1}-P2 construct. We further hypothesized that a single interprotomer disulfide bond (A120C-Q426C, iSS) is sufficient to maintain a prefusion-closed trimer, leading to a UFC_{M1}-P2-iSS construct. Lastly, we created a UFC_{M1}-P2-F_2C-VL construct, in which the shortened F_2 C-terminus (residues 87–92) was modified to remove buried charges, and the interprotomer disulfide bond (iSS) mutation was replaced with a hydrophobic contact (A120V/Q426L).

Four hMPV-F designs, UFC_{M1}, UFC_{M1}-P2, UFC_{M1}-P2-iSS, and UFC_{M1}-P2-F_2C-VL, were validated using the same procedure established for RSV-F. A Nickel column was used to capture all F species, whereas an IAC column was generated using NAb MPE8[63] to target the prefusion F in hMPV-F purification. For UFC_{M1}, Nickel purification yielded a trimer peak at ~11.9 ml in the SEC profile that was 5-fold higher than from an MPE8 column (Fig. 5a, left top), measured by ultraviolet absorbance at 280 nm (UV_{280}). DSC produced a thermogram with overlapping peaks, with T_{m1} and T_{m2} determined at 53.0°C and 59.6°C, respectively (Fig. 5a, left bottom). The Nickel/SEC-purified trimer fractions were analyzed by nsEM, in which no 2D classes of prefusion-closed trimers were identified (Fig. 5a, right). Meanwhile, no postfusion molecules were found in the EM micrographs. For UFC_{M1}-P2, the P2 mutation between β3 and β4 notably increased the hMPV-F yield, as shown by the SEC profile following Nickel purification (Fig. 5b, left top). DSC generated comparable thermal parameters with ~1 °C higher T_{m1} and T_{onset} (Fig. 5b, left bottom). All 2D classes obtained from nsEM corresponded to prefusion hMPV-F monomers with a similar shape to prefusion RSV-F monomers and contained no prefusion-closed trimers (Fig. 5b, right). UFC_{M1}-P2-iSS showed a lower yield after Nickel and MPE8 purification but with a higher ratio of prefusion-closed trimers within the total hMPV-F protein (Fig. 5c, left top). Furthermore, DSC demonstrated a single narrow peak with a single T_m of 72°C and T_{onset} of 58.3°C, which were substantially higher (by ~12–19 °C and ~13–14 °C, respectively) than the melting points of UFC_{M1} and UFC_{M1}-P2 (Fig. 5c, left bottom). Remarkably, almost all 2D classes in the nsEM analysis represented prefusion-closed hMPV-F trimers (Fig. 5c, middle), which was further confirmed by 3D reconstruction and structural fitting (PDB ID: 5WB0)[35] (Fig. 5c, right). The last construct, UFC_{M1}-P2-F_2C-VL, showed a low trimer yield after MPE8 purification, although a Nickel column produced a similar SEC profile to UFC_{M1} and UFC_{M1}-P2 (Fig. 5d, left top). The DSC thermogram contained two peaks: T_{m1} was comparable to those of UFC_{M1} and UFC_{M1}-P2, but T_{m2} increased to 83.6°C (Fig. 5d, left bottom). Interestingly, the nsEM analysis of Nickel/SEC-purified trimer fractions indicated the presence of prefusion-closed trimers, partially open trimers, and misfolded hMPV-F (Fig. 5d, middle). The 3D reconstruction revealed a tightened trimer apex and widening around the base, suggesting an intermediate fusion state (Fig. 5d, right). In reducing SDS-PAGE, the crosslinked hMPV-F protein produced monomer, dimer, and trimer bands on the gel for all four constructs except UFC_{M1}-P2-iSS, which displayed a single trimer band (Fig. S6c).

To further characterize UFC_{M1}-P2-iSS, we performed nsEM analyses of purified protein in complex with Fabs MPE8[63] and 101F[78]. The 3D reconstruction showed three MPE8 Fabs binding laterally to site III of a prefusion-closed trimer (Fig. 5e). The 3.25 Å-resolution cryo-EM model (EMDB-28891) of a recently reported hMPV-F design (v3B Δ12_D454C-V458C) bound to three single-chain variable fragments (scFv) of MPE8[60] could be fitted into the EM density with an excellent match. The nsEM analysis indicated stronger 101F binding to UFC_{M1}-P2-iSS, with more 2D classes showing two to three 101F Fabs binding to the hMPV-F trimer (Fig. 5f, left). Indeed, a 3D reconstruction with more structural detail was obtained for the 101F complex (Fig. 5f, right). The structural fitting of an hMPV-F/101F model revealed an upward angle of approach for 101F, which targets the exposed site IV. Altogether, our results indicate that UFC_{M1}-P2-iSS can preserve important neutralizing epitopes on the prefusion-stabilized hMPV-F trimer.

Antigenicity of the four UFC_{M1} constructs was evaluated by ELISA and BLI using five NAbs with known complex structures, ADI-61026[65], MPE8[63], 101F[78], DS7[85], and MPV458[66]. In the ELISA (Fig. 5g, Fig. S6d), all four UFC_{M1} constructs yielded comparable affinity for the site Ø-specific NAb, ADI-61026, with EC_{50} values of 0.0034–0.0042 μg/ml (Fig. 5g, Fig. S6d). The results indicated that our hMPV-F base construct, UFC_{M1}, and its derivatives adopt prefusion conformations, regardless of the trimer being open or closed. Notably, the hMPV-F UFC_{M1} series bound to ADI-61026 with similar EC_{50} values to the RSV-F UFC_{R1} series binding to the site Ø-specific D25 (0.0030–0.0061 μg/ml). Among these four constructs, UFC_{M1}-P2-iSS bound preferably to MPE8 with a 3.5–5.7-fold lower EC_{50} than other UFC_{M1} constructs, consistent

https://doi.org/10.1038/s41467-024-54287-x

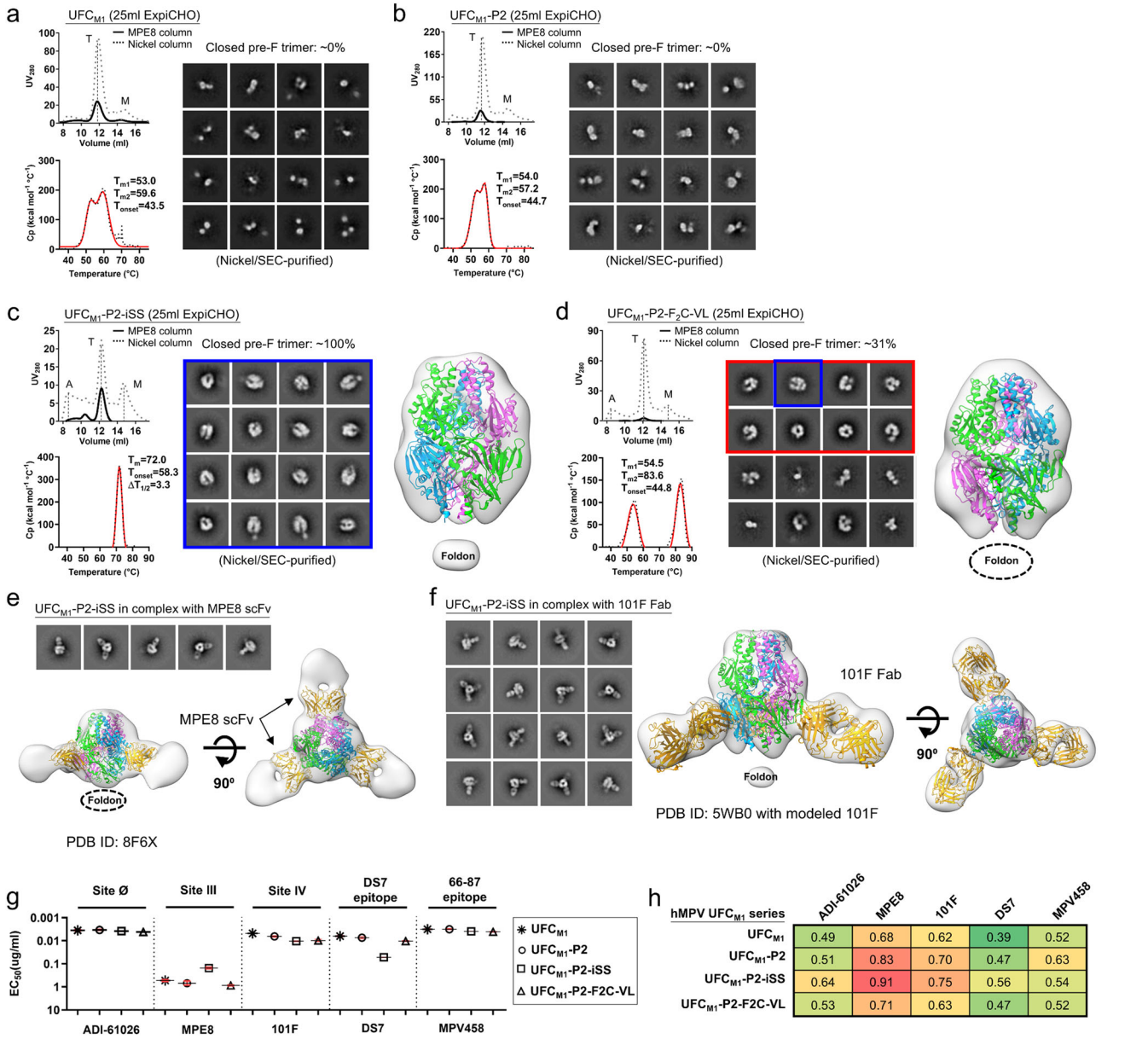

Fig. 5 | Design and in vitro characterization of hMPV-F UFC_{M1} series. SEC profile (left top), DSC profile (left bottom), representative 2D classification images (middle, or right when no 3D models shown), and 3D reconstruction from nsEM analysis (right) for (**a**) UFC_{M1}, (**b**) UFC_{M1}-P2, (**c**) UFC_{M1}-P2-iSS, and (**d**) UFC_{M1}-P2-F_2C-VL. All UFC_{M1} constructs were transiently expressed in 25 ml of ExpiCHO cells and purified using an MPE8 antibody column and a Nickel column, as all constructs contain a His_6 tag. The trimer (T) peak is marked on the profile. **e** The nsEM analysis of UFC_{M1}-P2-iSS bound to antibody MPE8. Representative 2D classification images are shown on the top, and side and top views of 3D reconstruction of the complex are shown on the bottom left and right, respectively. A 3.25 Å-resolution cryo-EM model of MPE8 scFv-bound v3B Δ12_D454C-V458C (PDB ID: 8F6X) was used for density fitting. **f** The nsEM analysis of UFC_{M1}-P2-iSS bound to antibody 101F. Representative 2D classification images are shown on the left, and side and top views of 3D reconstruction of the complex are shown on the right. A model of 101F Fab modeled onto a prefusion hMPV-F trimer (PDB ID: 5WB0) was used for density fitting. **g** ELISA-derived EC_{50} (μg/ml) values of four UFC_{M1} constructs binding to four antibodies, as in Fig. 1e. **h** BLI-derived antigenic profiles of four UFC_{M1} constructs binding to four antibodies. Sensorgrams were obtained using the same protocol as in Fig. 1f and are shown in Fig. S6e. The matrix of peak values at the highest antigen concentration is shown as in Fig. 1f.

with the fact that MPE8 interacts with two protomers of a prefusion-closed trimer. UFC_{M1}-P2-iSS exhibited the lowest affinity for DS7, with a 5.0–8.3-fold difference in EC_{50} compared with other UFC_{M1} constructs. Further analysis of the DS7 complex structure (PDB ID: 4DAG)[85] revealed that its binding requires the displacement of β22, which only occurs in monomers or open trimers. The four hMPV-F constructs exhibited similar binding affinities for NAbs 101F and MPV458 (Fig. 5f, Fig. S6d). Overall, BLI demonstrated consistent patterns compared with ELISA, with UFC_{M1}-P2-iSS showing the highest binding to ADI-61026 and MPE8 (Fig. 5g, Fig. S6e).

Crystallographic characterization of the hMPV-F UFC_{M1}-P2-iSS trimer

We obtained a 6 Å-resolution structure for ExpiCHO-expressed, Nickel/SEC-purified UFC_{M1}-P2-iSS using similar crystallization conditions to the first crystal structure of a prefusion hMPV-F design, 115-BV[35] (Tables S5, S6). The UFC_{M1}-P2-iSS structure was superimposed onto the 115-BV structure (PDB ID: 5WB0) for comparison (Fig. 6a). In the asymmetric unit, UFC_{M1}-P2-iSS adopted the same form as 115-BV, enabling the trimer structure to be modeled in a similar manner. UFC_{M1}-P2-iSS yielded a Cα-RMSD of 1.22 Å relative to 115BV at the

https://doi.org/10.1038/s41467-024-54287-x

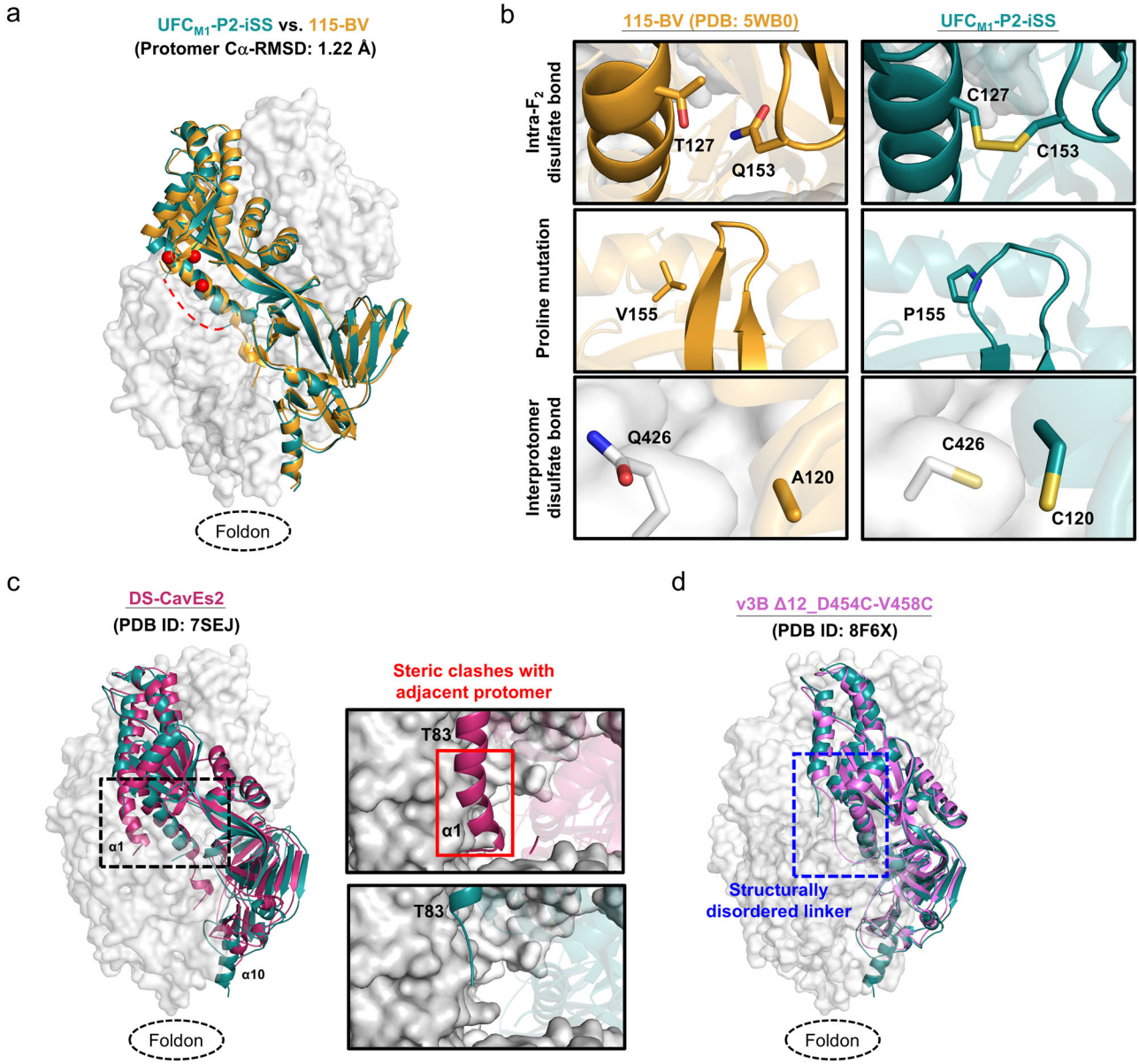

Fig. 6 | Crystallographic analysis of hMPV-F UFC$_{M1}$-P2-iSS. a The crystal structure of UFC$_{M1}$-P2-iSS (6.0 Å) is superimposed onto that of 115-BV (PDB ID: 5WB0), which are shown as green and gold ribbon models, respectively, within the gray trimer surface. Due to the limited resolution, structural details cannot be determined for the F_2-F_1 linker, A344-S347, or V442-E457. A red dotted line is added to show the expected approximate location of the missing F_2-F_1 linker. **b** Structural details of the intra-F_2 disulfide bond T127C-Q153C, the V155P (P2) mutation inserted into the β3/β4 hairpin tip for destabilizing the postfusion state, and the interprotomer disulfide bond A120C-Q426C (iSS) are shown in the top, middle, and bottom insets, respectively. The crystal structure of 115-BV is included for comparison. **c** The crystal structures of UFC$_{M1}$-P2-iSS and DS-CavEs2 (PDB ID: 7SEJ) are superimposed and shown as green and rouge pink ribbon models, respectively, within the gray trimer surface. The extended α1 helix in DS-CavEs2 that will clash with an adjacent protomer in a prefusion-closed trimer is circled in a black dotted line box. Close-up views of this region in DS-CavEs2 and UFC$_{M1}$-P2-iSS are shown in the right insets. **d** Crystal structures of UFC$_{M1}$-P2-iSS and v3B Δ12_D454C-V458C (PDB ID: 8F6X) are superimposed and shown as green and pink ribbon models, respectively, within the gray trimer surface. The F_2-F_1 linker region is circled in a blue dotted line box.

protomer level. The three key elements of the UFC$_{M1}$-P2-iSS design were compared to 115-BV, which has the most complete F structure bearing minimum mutations (Fig. 6b). The T127C-Q153C mutation was found to be critical to maintain prefusion hMPV-F, with a Cα-Cα distance of 6.8 Å in the DS-CavEs2 structure[61]. From the fitted model, this disulfide bond had an estimated Cα-Cα distance of 6.3 Å in UFC$_{M1}$-P2-iSS, compared with a Cα-Cα distance of 7.2 Å between T127 and Q153 in 115-BV (Fig. 6b, top). The V155P mutation appears to widen the β3-β4 turn in UFC$_{M1}$-P2-iSS, which would likely facilitate disulfide bond formation at positions 153 to 127 and destabilize postfusion F (Fig. 6b, middle). The interprotomer disulfide bond (C120-C426) had an estimated Cα-Cα distance of 5.8 Å, thus locking hMPV-F in a prefusion-closed trimer conformation (Fig. 6b, bottom). Because of the limited resolution, the structure could not be resolved for the F_2-F_1 linkage, part of α8 (A344-S347), and part of α9-α10-β23 (V442-E457) (Fig. S7).

The UFC$_{M1}$-P2-iSS structure was then compared to two leading prefusion hMPV-F designs: DS-CavEs2[61] and v3B Δ12_D454C-V458C[60]. The structural superposition of UFC$_{M1}$-P2-iSS and DS-CavEs2 (PDB ID: 7SEJ) revealed differences in the stalk and α1 helix. Compared with a well-formed α10 helix in UFC$_{M1}$-P2-iSS, DS-CavEs2 showed an incomplete α10 helix because of the intra-F_1 disulfide bond (T365C-V463C) between β14 and α10, which destabilizes the C-terminal trimeric stalk (Fig. 6c, left). This may also explain why DS-CavEs2 crystalized as a monomer with an extended α1 helix that would clash with the adjacent

protomer in a prefusion-closed trimer (Fig. 6c, right). Nonetheless, two cryo-EM structures showed trimeric DS-CavEs2 in complex with NAbs that interact with two protomers at the trimer interface, although the α10 helix was partially unstructured[65,67]. UFC_{M1}-P2-iSS was then structurally superimposed onto v3B Δ12_D454C-V458C (PDB ID: 8F6X) (Fig. 6d). Both designs showed similar cleavage site linker structures, but the trimer base (β23 and α10) in v3B Δ12_D454C-V458C adopted a non-native conformation because of the unintended intraprotomer disulfide bond (D454C-V458C)[60]. In summary, our crystal structure, despite its modest resolution, validated the UFC_{M1}-P2-iSS design and allowed structural comparisons with previously reported hMPV-F designs.

Potent pneumovirus-neutralizing antibodies identified by RSV-F UFC_{R1}-P2-NQ

As most children are infected by RSV before the age of two and will be reinfected throughout their adulthood[86], the healthy adult population offers a rich source of RSV NAbs. We hypothesized that if our lead RSV-F design, UFC_{R1}-P2-NQ, can identify prefusion-specific RSV NAbs from a human antibody library, then it may induce similar NAbs in vaccination (Fig. 7a). Following our previously established protocol[87], we constructed a large phage-display scFv library using peripheral blood mononuclear cells (PBMCs) from 10 healthy donors and performed biopanning experiments to screen this human scFv library using UFC_{R1}-P2-NQ as an antigen probe. After four biopanning steps, 96 clones were randomly selected for phage ELISA against sc9-10 DS-Cav1, a disulfide-locked prefusion-closed RSV-F trimer[44]. A total of 36 scFv clones were sequenced (Fig. S8a), and eight with complete variable regions were selected as representative clones (Fig. S8b). Sequence analysis revealed that these eight clones are derived from five heavy chain variable (V_H) genes and five λ/κ-light chain variable (V_L/V_K) genes (Fig. 7b, Fig. S8c). All eight clones in the scFv-Fc form could be expressed in HEK293 F cells with high yield except F1.

These eight clones were evaluated in an ELISA against RSV-F using sc9-10 DS-Cav1[44] and hMPV-F using UFC_{M1}-P2-iSS (Fig. 7c, Fig. S8d). In the scFv-Fc form, A4, D1, and F3 showed higher affinities for sc9-10 DS-Cav1 than other RSV-F reactive clones, such as E3, E5, and H9, with a ~ 4.8- to 18.9-fold difference in EC_{50}. The binding affinities of A4, D1, and F3 scFv-Fc antibodies were largely comparable to D25 IgG[42]. In the IgG form, these three clones displayed similar affinities for sc9-10 DS-Cav1 that were, however, slightly lower than that of D25, with a 2.9- to 3.9-fold difference in EC_{50}. When tested against UFC_{M1}-P2-iSS, only D1 and F3 exhibited any measurable binding to this prefusion hMPV-F trimer. Specifically, D1 and F3 had similar affinities for hMPV-F in the scFv-Fc form, which were reduced 25- and 3.8-fold, respectively, when changed to the IgG form. These phage library-derived antibodies demonstrated different potencies in live RSV and hMPV neutralization assays (Fig. 7d, Fig. S8e). In the scFv-Fc form, A4 appeared to be the best RSV neutralizer, with a half maximal inhibitory concentration (IC_{50}) of 0.0021 μg/ml, 1.8-fold higher than a highly optimized therapeutic antibody, MEDI8897 (Nirsevimab)[38,88]. In the IgG form, A4 showed a nearly identical IC_{50} to MEDI8897, F3 yielded a comparable IC_{50} to D25 (0.013 μg/ml *vs.* 0.011 μg/ml, respectively), and D1 exhibited similar potency to a site II-directed NAb, Motavizumab[89]. Both D1 and F3 IgGs neutralized live hMPV, with F3 showing ~11-fold higher potency, estimated by the IC_{50} value, than a widely studied cross-NAb, MPE8[63].

To understand how these functional antibodies were selected during the biopanning process, we pooled the pre-panning and four post-panning scFv libraries for next-generation sequencing (NGS) on the Ion GeneStudio S5 platform using an Ion 530 chip. NGS yielded over ~18.8 million raw reads, which were processed using the Antibodyomics 2.0 pipeline[87] to generate full-length V_H and $V_{L/K}$ reads for bioinformatics analyses (Fig. S8f). A distinct pattern of antibody enrichment and rapid convergence after two panning rounds were observed in the quantitative library profiles (Fig. 7e, Fig. S8g). In terms of germline gene usage, IGHV3 and IGLV1 accounted for 97% and 64% of the converged library, respectively, consistent with the finding that six of eight selected scFv clones were derived from the combination of these two genes (Fig. 7b). In terms of somatic hypermutation (SHM), both V_H and $V_{L/K}$ distributions shifted from a germline-like (SHM: 1–3%) pre-panning population toward a more mature population after convergence, peaking at 11–13% and 7–9%, respectively. In terms of heavy chain complementarity-determining region 3 (HCDR3) length, the converged library contained two prevalent scFv families with 7–9 aa (22.9%) and 15–17 aa (45.2%) HCDR3 loops, compared with a normal distribution with an average of 13 aa in the pre-panning library. The κ-light chains showed little change in germline gene usage, SHM, and κ-chain CDR3 (LCDR3) length (Fig. S8g), suggesting that κ-light chains were not used by RSV-specific scFv clones. A 2D identity-divergence analysis was then conducted to visualize the scFv-derived heavy- and light-chain (HC and LC, respectively) populations during biopanning (Fig. 7f and Fig. S8h). The 2D plots revealed the rapid enrichment of D1, E3, and D12 clones and modest expansion of A4, F3, and E5 clones after two panning steps, but little selection pressure was noted for F1 and H9. Between the two most potent neutralizers, F3 exhibited more pronounced expansion than A4, which accounted for 1.0% and 0.03% of their germline gene families, respectively.

Structural characterization of RSV- and hMPV-neutralizing human antibodies

Of the eight scFv clones, A4, D1, and F3 displayed distinct binding and neutralization profiles. To investigate how these human antibodies recognize prefusion RSV-F, we generated A4, D1, and F3 Fabs and formed complexes with sc9-10 DS-Cav1[44] for structural analysis. We first used nsEM to identify their epitopes on the prefusion trimer (Fig. 8a, b). For A4, the 2D classification revealed sc9-10 DS-Cav1 trimers with Fabs bound to an epitope near the trimer apex (Fig. 8a, left). Compared with the 2D classes obtained for the D25-bound UFC_{R1}-P2-NQ trimer (Fig. 2e, left), A4 shifted sideward and created a larger angle relative to the trimer axis in the side views (Fig. 8a, left). The visual inspection of previously reported RSV-F NAbs revealed that a germline version of NAb RSD5 (RSD5-GL) in complex with DS-Cav1 (PDB ID: 6DC3[51]) could be fitted into the A4/sc9-10 DS-Cav1 density with a nearly perfect match (Fig. 8a, right). The crystal structure (PDB ID: 6DC3) revealed a distinctive RSD5 epitope[51] that mainly overlaps with site Ø, as defined by D25[42], but also extends to site V, as defined by hRSV90[47], 01.4B, and ADI-14442[52]. For D1 and F3, nsEM revealed an angle of approach resembling that of the site III-specific NAb, MPE8[63] (Fig. 8b, left), which was confirmed by fitting the MPE8/DS-Cav1 complex[63] into the nsEM densities of D1- and F3-bound sc9-10 DS-Cav1 (Fig. 8b, right). The MPE8-like epitope specificity also explained their reactivity with both RSV-F and hMPV-F.

Given the high potency of A4 and its similar angle of approach compared with RSD5[51], we examined the gene families of these two NAbs (Fig. 8c). Consistent with the same binding and approach angle, A4 and RSD5 appeared to originate from the same V_H-V_L combination (IGHV3-30*01-IGLV2-14*03), showing CDR3 sequence identities of 78% (14/18) and 50% (5/10) for HC and LC, respectively. This finding suggests that RSD5 and A4 may belong to a "public" antibody lineage targeting this unique epitope that overlaps both sites Ø and V. Similar public antibody lineages have been reported for SARS-CoV-2[90–92]. We obtained a crystal structure for A4 scFv-bound UFC_{R2}-iSS-P2-NQ (Table S7). The RSD5-GL/DS-Cav1 structure (PDB ID: 6DC3)[51] was used as a template to build the A4/UFC_{R2}-iSS-P2-NQ complex structure by molecular replacement, which was refined to a final model with a resolution of 4.0 Å (Fig. 8d, top left). At this resolution, charged or long aliphatic side chains could not be modeled as accurately as aromatic side chains. Nonetheless, our crystal structure revealed a tightly packed interface with more than 10 potential hydrogen bonds based

https://doi.org/10.1038/s41467-024-54287-x

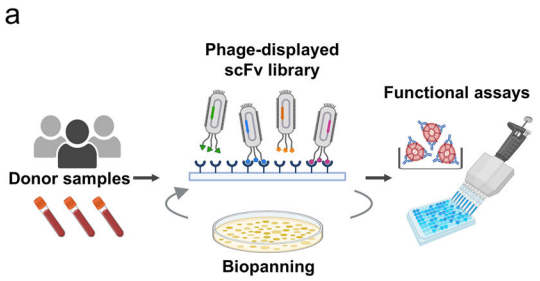

b

RSV antibodies isolated from a normal donor scFv antibody library. [a]

Clone [c]	V_H family	V_H identity (%)	$V_{L/K}$ family	$V_{L/K}$ identity (%)	Yield (mg/l) [b]
IXL-D1	IGHV3-21*01	87.8%	IGLV1-40*01	67.0	61.6
IXL-E3	IGHV3-21*01	88.5	IGLV1-40*01	93.1	64.0
IXL-F3	IGHV3-21*01	87.5	IGLV1-40*01	92.7	86.6
IXL-D12	IGHV3-66*01	99.3	IGLV1-40*01	96.2	50.6
IXL-E5	IGHV3-30*18	94.4	IGLV1-51*01	97.9	82.4
IXL-A4	IGHV3-30*14	88.9	IGLV2-14*03	95.5	76.4
IXL-F1	IGHV1-69*01	94.4	IGLV6-57*03	97.3	0.34
IXL-H9	IGHV3-43*02	89.6	IGKV1-39*01	98.6	44.4

[a] Gene analysis was performed using the IMGT/V-quest server (https://www.imgt.org/IMGT_vquest).
[b] In initial evaluation, the eight antibodies were changed to the His-tagged scFv-Fc form, expressed transiently in HEK293 F cells, and purified using a Nickel column.
[c] The official clone name combines library name (XL) and scFv Index.

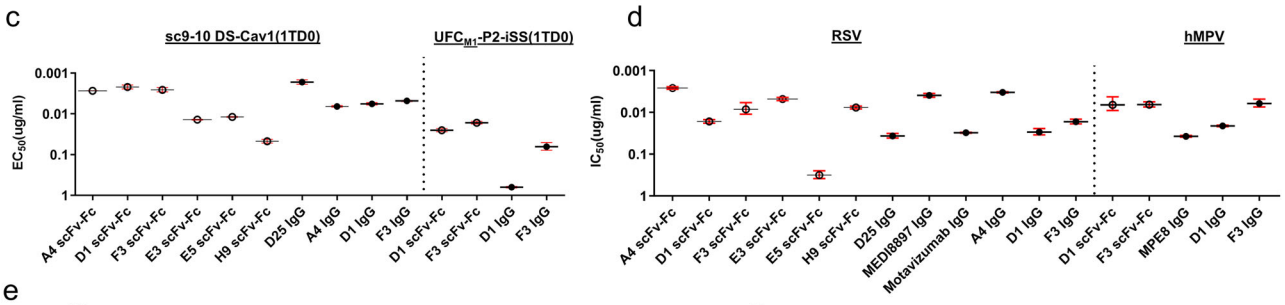

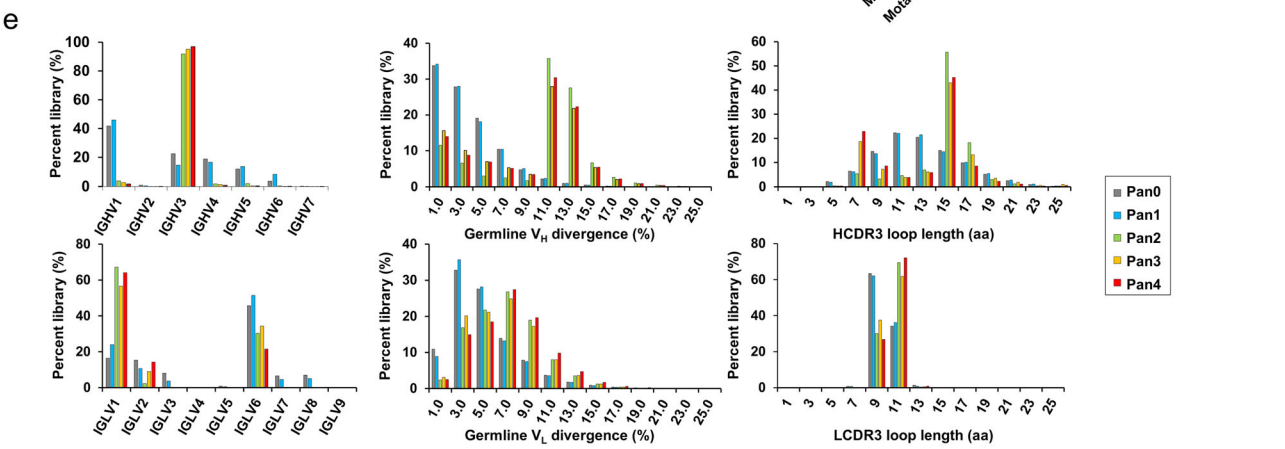

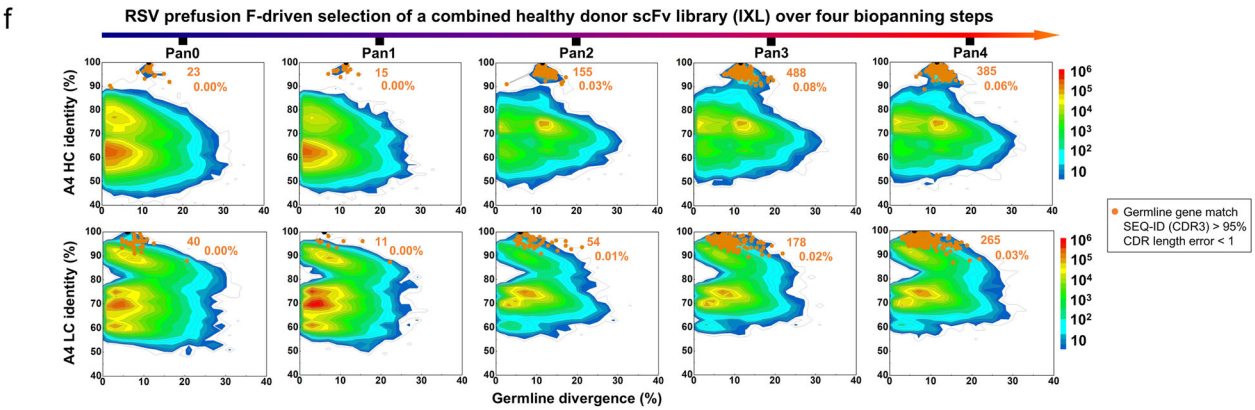

Fig. 7 | Potent pneumovirus neutralizing antibodies identified from a human antibody library. a Schematic representation of the phage display workflow. **b** Gene family analysis of eight scFv clones identified from a phage-displayed human antibody (scFv) library using RSV-F UFC$_{R1}$-P2-NQ as a biopanning antigen. **c** ELISA-derived EC$_{50}$ (μg/ml) values of library-derived antibodies binding to RSV-F sc9-10 DS-Cav1 and hMPV-F UFC$_{M1}$-P2-iSS. **d** IC$_{50}$ (μg/ml) values derived from live RSV and hMPV neutralization assays. Error bars in (**c**, **d**) represent the difference between duplicates at each concentration tested for each sample. **e** Distribution of germline gene usage, somatic hypermutation, and CDR3 length plotted for heavy chains (HCs) and λ-light chains (λ-LCs) of the scFv library during the biopanning process. **f** Identity-divergence analysis of the IXL-A4 (or A4) within the scFv library during the biopanning process. The sequence datasets used in (**e**) and (**f**) were obtained from next-generation sequencing (NGS) of the scFv libraries on an Ion GeneStudio S5 platform. For the heatmaps in (f), after data processing using an Antibodyomics pipeline, each sequence is plotted as a function of sequence identity from a reference antibody chain and sequence divergence from the assigned germline gene. Color indicates sequence density at a particular point on the 2D plot. Sequences with the same germline gene, a CDR3 identity ≥95%, and a 1-residue error margin of CDR length calculation relative to the reference antibody chain are plotted as orange dots with the number of sequences and gene family percentage labeled. The schematic representation of phage-based antibody isolation was created in BioRender. Lee, Y. (2024) BioRender.com/p25x130.

https://doi.org/10.1038/s41467-024-54287-x

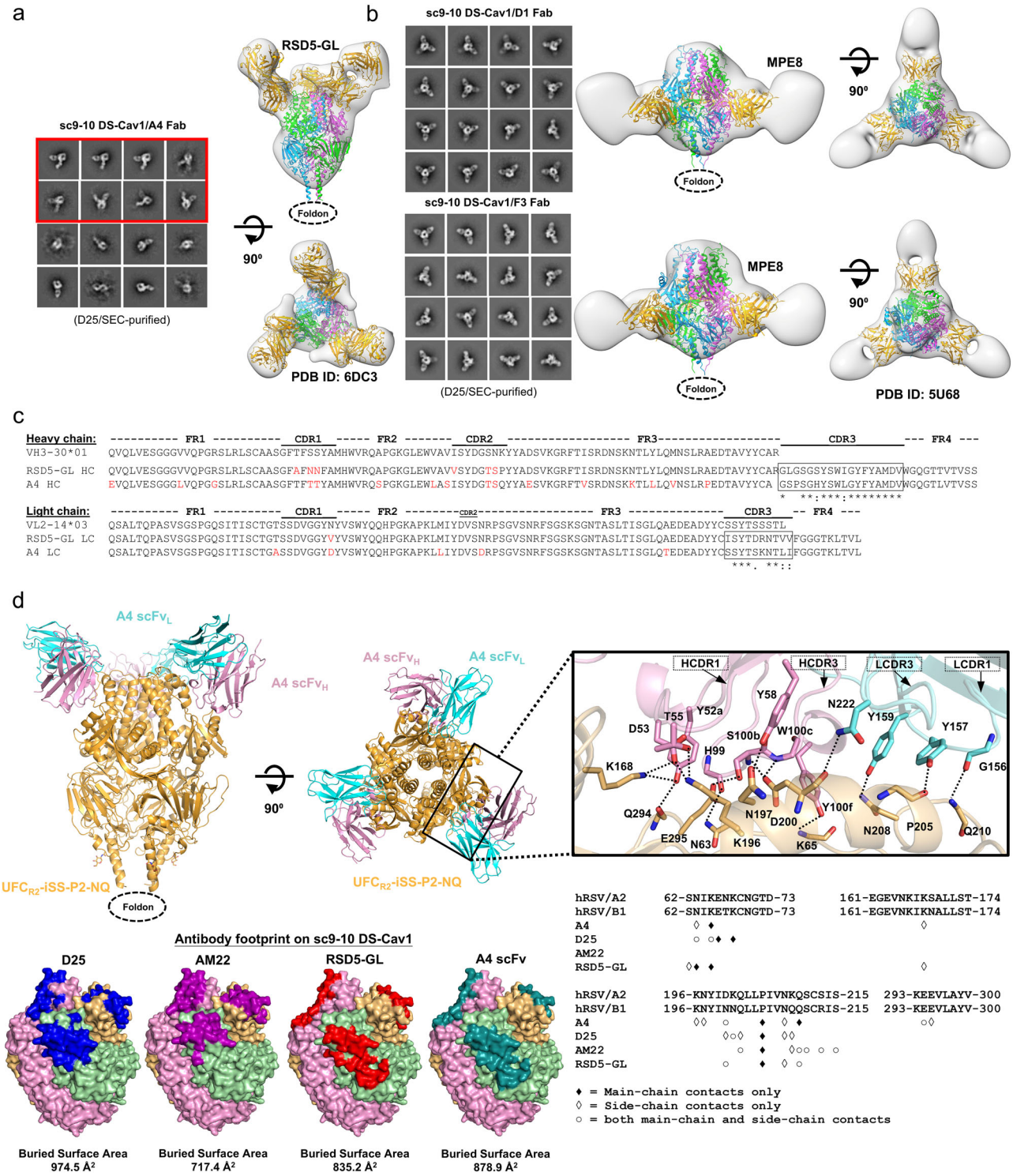

Fig. 8 | Structural characterization of potent pneumovirus neutralizing human antibodies. a The nsEM analysis of sc9-10 DS-Cav1 in complex with A4. Representative 2D classification images are shown on the left, and side and top views of 3D reconstruction of the complex are shown on the right. A 3.50 Å-resolution crystal structure of RSD5-bound DS-Cav1 (PDB ID: 6DC3) was used for density fitting. The 2D classification images containing two or more than two bound A4 Fabs are circled in a red line box. **b** The nsEM analysis of sc9-10 DS-Cav1 in complex with D1 and F3. Representative 2D classification images are shown on the left, and side and top views of 3D reconstruction of the complex are shown on the right. A 3.08 Å-resolution crystal structure of MPE8-bound DS-Cav1 (PDB ID: 5U68) was used for density fitting. **c** Sequence analysis of A4 and RSD5 heavy and light chains with alignment to respective germline genes. Mature antibody residues that differ from the germline are colored in red. **d** Crystallographic analysis of UFC$_{R2}$-iSS-P2-NQ in complex with A4 scFv and structural epitope mapping. Top left: A 4.0 Å-resolution crystal structure UFC$_{R2}$-iSS-P2-NQ in complex with A4 scFv is shown as ribbon models, with UFC$_{R2}$-iSS-P2-NQ in gold and A4 heavy and light chains in pink and cyan, respectively. Top right: Close-up view of the A4/RSV-F interface. Side chains are shown for residues involved in hydrogen bond interactions across the A4/RSV-F interface, which were identified based on the estimated donor-acceptor distances and are indicated by dotted black lines. HCDR1, HCDR3, LCDR3, and LCDR1 loops are indicated. Bottom left: Surface models of prefusion RSV-F trimer showing footprints of D25, AM22, RSD5, and A4 colored in blue, rouge pink, red, and teal blue, respectively. Bottom right: RSV-F sequence with antibody-interacting residues labeled for D25, AM22, RSD5, and A4. Three types of contact are considered using a cutoff distance of 5 Å: main-chain contacts, side-chain contacts, and both.

on the estimated donor-acceptor distances (Fig. 8d, top right). Specifically, A4 employs HCDR1 (4 residues), HCDR3 (4 residues), LCDR1 (3 residues), and LCDR3 (1 residue) to interact with key residues of the RSV-F α4 helix (site Ø), such as K196, N197, D200, L204, P205, N208, and Q210 (n.b., the helix kinks at residue 203 prior to P205). Additional contacts were made with N63, K65 (β2-α1 loop, site Ø), K168 (α3), E294, and E295 (β5-β6 turn) of surrounding structural elements. The superimposition of A4/UFC_{R2}-iSS-P2-NQ and RSD5-GL/DS-Cav1 using various fitting schemes revealed closely matched RSV-F α4 helices in site Ø and antibody HCDR3 loops (Fig. S9a). When the Cα atoms of α4 residues L195-L207 were used for fitting, we obtained a Cα-RMSD of 1.0 Å for HCDR3 (13 residues, H100-V102 for A4 and S100-V102 for RSD5-GL), which formed nearly identical interactions with RSV-F (Fig. S9b). Using the PDBePISA webtool[93], the A4 footprint on RSV-F was also compared with those of D25[42], AM22, and RSD5-GL[51], showing the closest match to the RSD5-GL footprint (Fig. 8d, bottom left). Further analysis indicated that A4 appears to engage more residues on RSV-F than D25, AM22, and RSD5-GL, interacting with 12, 10, 7, and 8 residues, respectively, using both backbone and sidechain contacts (Fig. 8d, bottom right). Our structure thus provided critical insights into how A4 interacts with RSV-F to achieve a comparable potency to MEDI8897 (Nirsevimab)[38,88].

Antibody responses induced by rationally designed RSV-F trimer vaccines in mice

We assessed the immunogenicity of seven RSV-F constructs, including four UFC designs (UFC_{R1}-P2-NQ/-L2 and UFC_{R2}-P2-NQ/-L2) and three "control" designs (DS-Cav1Δp27 (Fig. S1i-S1j), SC-TM[33], and sc9-10 DS-Cav1[44]), in BALB/c mice (Fig. 9a). DS-Cav1Δp27 and sc9-10 DS-Cav1 were purified using a D25 antibody column, whereas SC-TM-His_6 was purified on a Nickel column, all further processed by SEC to isolate the trimer fractions. A mouse immunization protocol used in our previous vaccine studies[79,94,95] was adopted with the number of animals per group increased to 10 to improve power in the statistical analysis. RSV-F antigens were formulated with AddaVax, an oil-in-water emulsion adjuvant, and administered intradermally through footpad injections (4 footpads, 2.5 μg/footpad) at 3-week intervals. Serum was isolated from blood draws 2 weeks after each immunization for quantitative serological analysis.

Serum binding antibody responses were determined using a sc9-10 DS-Cav1 1TD0 probe in ELISA, with EC_{50} titers calculated for comparison (Fig. 9b, Fig. S10a, b). Prefusion RSV-F has been widely used as a coating antigen in serum ELISA[25,43,96,97]. Sc9-10 DS-Cav1[44] provides the most suitable antigen for probing the prefusion-specific binding antibody response, as it produces ~100% closed trimers, contains all major NAb epitopes (including sites II, III, and IV present in both prefusion and postfusion states), and does not bind to the postfusion-specific antibody ADI-14359. This probe, however, does not provide information on the antibody response to site I. Overall, all groups demonstrated comparable binding antibody titers at each of the four studied time points except the SC-TM-His_6 group, which showed significantly lower EC_{50} titers in most cases. This pattern was noted as early as week 2, where SC-TM-His_6 showed a 7.1- to 28.7-fold lower EC_{50} titer than other antigens. Sc9-10 DS-Cav1 elicited the highest binding antibody titers at week 5, showing 3.6- and 46.1-fold higher EC_{50} titers than DS-Cav1Δp27 and SC-TM-His_6, respectively. Among our four designs, UFC_{R2}-P2-L2 showed the highest EC_{50} titer at week 5, which was 3.1- and 39.6-fold higher than DS-Cav1Δp27 and SC-TM-His_6, respectively. Most mouse groups reached saturated EC_{50} titers after three immunizations at week 8. Interestingly, although UFC_{R1}-P2-NQ and UFC_{R1}-P2-L2 showed lower binding antibody titers than their UFC_{R2} counterparts at week 2, this pattern changed at week 5 and was reversed at weeks 8 and 11. Furthermore, L2 outperformed NQ regardless of the base construct, UFC_{R1} or UFC_{R2}, at all four time points. These results correlated with the ratio of prefusion-closed trimers obtained from nsEM (Figs. 1, 2, 4). The week-11 sera were also analyzed against hMPV-F using the UFC_{M1}-P2-iSS(1TD0) probe (Fig. 9c, Fig. S10c). A few mice in the DS-Cav1Δp27, SC-TM-His_6, and sc9-10 DS-Cav1 groups showed nonspecific signals, indicated by absorbance at 450 nm (A450).

Serum NAb responses were assessed using a live RSV neutralization assay[98], with the 50% inhibitory dilution (ID_{50}) calculated for comparison. None of the RSV-F vaccines elicited a detectable NAb response at week 2 except for one mouse in the UFC_{R1}-P2-L2 group, but the ID_{50} titers were detectable at weeks 5, 8, and 11 and continued to increase throughput these timepoints (Fig. 9d, Fig. S10d, S10e). Consistent with the binding antibody titers, the DS-Cav1Δp27 and SC-TM-His_6 groups showed the lowest NAb titers across all timepoints. In contrast, sc9-10 DS-Cav1 yielded the highest NAb titers of 7154, 10017, and 21936 at weeks 5, 8, and 11, respectively, which were 7.6-, 2.4-, and 11.5-fold higher than the NAb titers elicited by DS-Cav1Δp27. Among our four designs, the UFC_{R1}-P2-NQ group showed the highest ID_{50} titer at week 8, which was comparable to the sc9-10 DS-Cav1 group. At weeks 8 and 11, the two UFC_{R2} designs consistently underperformed their UFC_{R1} counterparts in terms of ID_{50} titers. These results confirmed that a high ratio of prefusion-closed trimers (e.g., 73% for UFC_{R1}-P2-NQ) (Fig. 2c) may benefit the elicitation of potent NAbs but also demonstrated that the L2 mutation, which transiently exposes site I, may dampen NAb responses (Figs. 2f, 4f). Serum neutralizing activity (ID_{50} titer) and binding activity (EC_{50} titer) demonstrated a positive correlation, with a coefficient of determination $R^2 = 0.7504$ or a coefficient of correlation $R = 0.8663$, suggesting that the antibodies binding to the prefusion-closed RSV-F trimers contribute most to serum neutralization (Fig. S10f). Lastly, the week-11 serum samples were tested using a live hMPV neutralization assay[99] (Fig. 9e, Fig. S10g). All groups showed negligible NAb responses against hMPV except SC-TM-His_6, likely caused by the weak NAbs induced by the postfusion form of this antigen.

Our results highlighted the advantage of stabilized, prefusion-closed RSV-F trimer in NAb elicitation. The first-generation DS-Cav1 and SC-TM induced low NAb titers in these experiments. Overall, sc9-10 DS-Cav1 appeared to be the best performer among all RSV-F constructs, with UFC_{R1}-P2-NQ ranked the second-best performer at most time points in the immunization.

Antibody responses induced by rationally designed hMPV-F trimer vaccines in mice

The immunogenicity of three hMPV-F design constructs, UFC_{M1}-P2, UFC_{M1}-P2-iSS, and UFC_{M1}-P2-F_2C-VL, was assessed in mice (Fig. 9a). The hMPV-F-specific binding antibody responses were measured by ELISA using a UFC_{M1}-P2-iSS(1TD0) probe for all timepoints. The EC_{50} titers were calculated and plotted longitudinally for comparison (Fig. 9f, Fig. S10h–S10i). Overall, all groups demonstrated strong binding antibody responses, with EC_{50} titers ≥ 9153 after two vaccine doses. The UFC_{M1}-P2 group reached the highest EC_{50} titer at week 5, comparable to the UFC_{M1}-P2-iSS group and 2.3-fold higher than the UFC_{M1}-P2-F_2C-VL group. Interestingly, the UFC_{M1}-P2-F_2C-VL group yielded higher EC_{50} titers than the other two groups at week 8. Cross-reactive antibody responses were assessed using week-11 sera against an RSV-F sc9-10 DS-Cav1 1TD0 probe (Fig. 9g, Fig. S10j). All three groups showed negligible signals except some nonspecific signals observed for the UFC_{M1}-P2 group. Live hMPV neutralization assays[99] were used to assess serum NAb responses elicited by various hMPV-F constructs (Fig. 9h and Fig. S10k–S10l). As expected, none of the three hMPV-F constructs elicited NAb responses against autologous hMPV at week 2. Importantly, the UFC_{M1}-P2-iSS group showed the most potent NAb titers, with ID_{50} titers of 33911, 37129, and 46408, which were 3.9-, 3.0-, and 2.1-fold higher than those elicited by UFC_{M1}-P2 at weeks 5, 8, and 11, respectively. This confirmed the importance of our rationally designed

https://doi.org/10.1038/s41467-024-54287-x

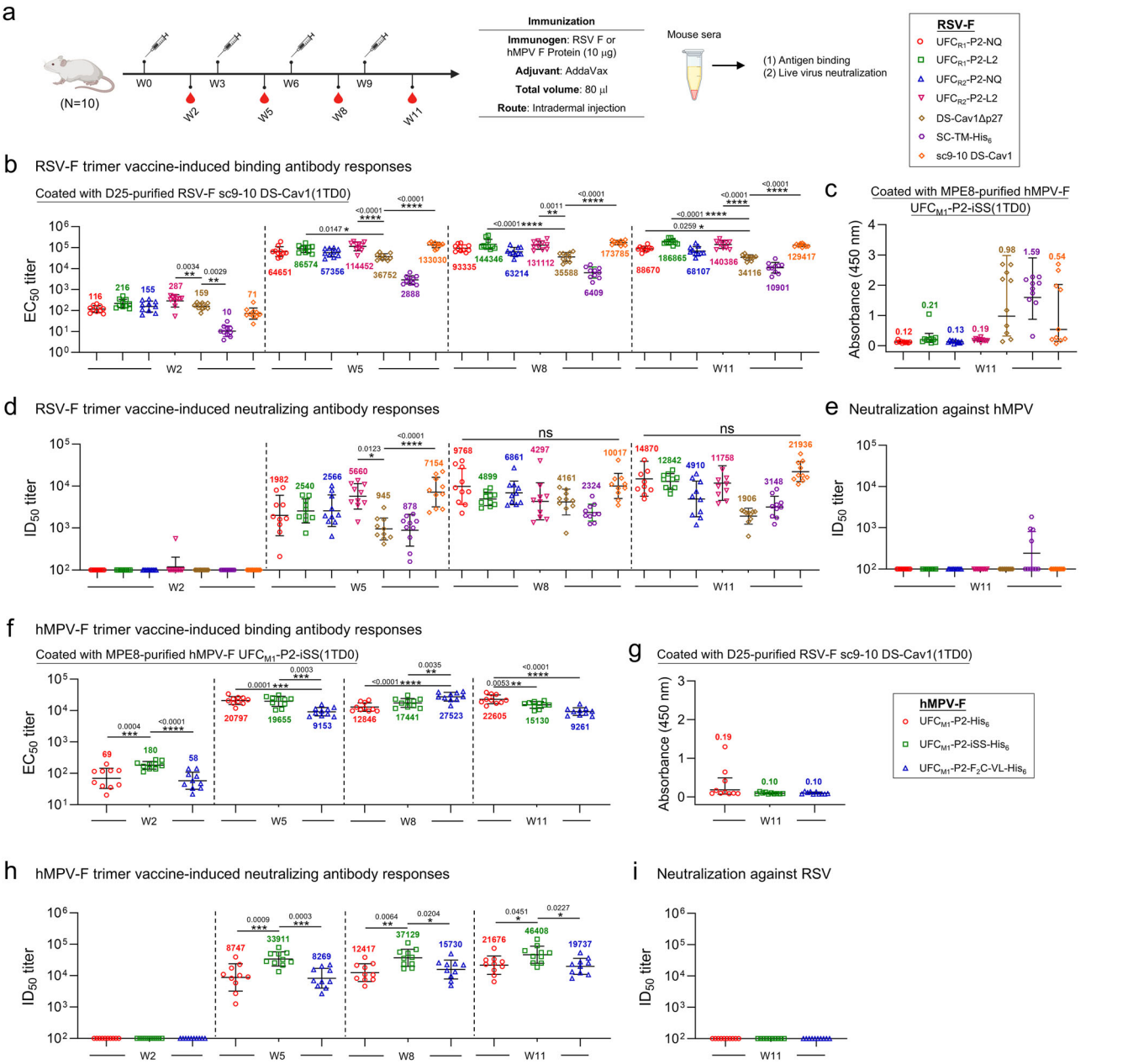

Fig. 9 | Antibody responses to rationally designed RSV and hMPV-F trimer vaccines in mice. a Schematic representation of the mouse immunization regimen for both RSV-F and hMPV-F vaccines ($n = 10$ mice/group). **b**, **c** RSV-F vaccine-induced binding antibody responses against RSV-F sc9-10 DS-Cav1(1TD0) and hMPV-F UFC$_{M1}$-P2-iSS(1TD0). **d**, **e** RSV-F vaccine-induced neutralizing antibody responses against live RSV-A2-GFP and live hMPV-GFP. In (**b**–**e**), DS-Cav1Δp27, SC-TM-His$_6$, and sc9-10 DS-Cav1 are included for comparison. **f**, **g** HMPV-F vaccine-induced binding antibody responses against hMPV-F UFC$_{M1}$-P2-iSS(1TD0) and RSV-F sc9-10 DS-Cav1(1TD0). **h**, **i** HMPV-F vaccine-induced neutralizing antibody responses against live hMPV-GFP and live RSV-A2-GFP. EC$_{50}$ titers (**b**, **c**, **f**, **g**) were derived from the ELISA analysis of mouse serum against coating antigens, with geometric mean EC$_{50}$ titers labeled on the plots. ID$_{50}$ titers were derived from the live RSV and hMPV neutralization assays, with geometric mean ID$_{50}$ values labeled on the plots. Notably, the ID$_{50}$ values were derived by setting the lower/upper constraints of % neutralization at 0.0/100.0. The data points are shown as mean ± SD. The data were analyzed using one-way ANOVA, followed by Tukey's multiple-comparison *post hoc* test for each timepoint. The statistical significance is indicated as the following: ns (not significant), $^{*}p < 0.05$, $^{**}p < 0.01$, $^{***}p < 0.001$, and $^{****}p < 0.0001$. In (**b**) and (**d**), statistical analyses of EC$_{50}$ and ID$_{50}$ values were performed by comparing individual RSV-F vaccine with the control, DS-Cav1Δp27. Detailed ELISA and neutralization data and the complete statistical analysis are shown in Fig. S10. The schematic representation of the mouse immunization protocol was created in BioRender. Zhang, Y. (2024) BioRender.com/o89v779.

mutations for producing a stabilized, prefusion-closed hMPV-F trimer, which in turn induced a potent NAb response against hMPV. We evaluated the cross-neutralizing activity of hMPV-F-induced mouse sera using live RSV assays, which did not detect NAb titers against RSV (Fig. 9i, Fig. S10m). Altogether, our results indicate that UFC$_{M1}$-P2-iSS, as a fully closed prefusion hMPV-F trimer, can induce a potent NAb response in mice.

Sex-dependent antibody responses induced by RSV-F and hMPV-F trimers

We investigated the influence of sex on vaccine-induced NAb responses using two leading vaccine candidates, UFC$_{R1}$-P2-NQ for RSV-F (Fig. S10n) and UFC$_{M1}$-P2-iSS for hMPV-F (Fig. S10o). Briefly, male mice were immunized following the same regimen as used for female mice (Fig. 9a). Serum samples collected after four injections at week 11 were

evaluated using live RSV or hMPV neutralization assays. For RSV, the UFC_{R1}-P2-NQ group showed a mean ID_{50} titer of 7091 in male mice that was notably lower than a titer of 14870 in female mice (Fig. S10n). A more pronounced sex-specific difference was observed in the hMPV study: the UFC_{M1}-P2-iSS group showed a mean ID_{50} titer of 8214 in male mice that was 5.6-fold lower than in female mice (Fig. S10o). Therefore, both RSV-F and hMPV-F trimer vaccines appeared to induce greater NAb responses in female mice than in male mice. This observation is consistent with the previous finding that females tend to develop stronger humoral responses than males following vaccination[100,101].

Discussion

Both RSV and hMPV cause LRT infections in infants, young children, and the elderly[1,2]. Although RSV-F and HMPV-F share only ~30% sequence identity, their F proteins are structurally similar in both prefusion and postfusion states[102]. Over the last decade, at least four rational RSV-F designs have been reported and extensively characterized in vitro and in vivo[33,43–45]. Some of these structurally optimized prefusion RSV-F constructs gave rise to the recently licensed RSV vaccines ABRYSVO (GSK)[54] and AREXVY (Pfizer)[45,103]. Inspired by the success of these RSV-F designs, similar structure-based design principles have been applied to hMPV-F to stabilize the prefusion trimer and facilitate vaccine development[60–62]. However, outcomes from these studies suggest that rational hMPV-F design is still in its infancy. As a result, there are no rationally designed hMPV-F trimer vaccines approved for human use.

The recently approved RSV vaccines have been celebrated as a success of structure-based rational vaccine design[41], but the cause of RSV-F metastability largely remains unclear. In addition, an in-depth comparative analysis of previous RSV-F designs has not been reported. Our study addressed these issues with a systematic approach. Notably, use of the site Ø-specific NAb D25[42] for purification allowed us to quantify and extract the prefusion fraction of RSV-F from mammalian cell expression. Both SC-TM and 847A had a low yield using a D25 NAb column but not a Nickel affinity column, suggesting the presence of non-prefusion F species. While x-ray crystallography validated our RSV-F designs in atomic detail, nsEM was extensively used to probe RSV-F structures and fusion states. Indeed, nsEM demonstrated that His-tagged SC-TM and 847A contained detectable postfusion F trimers after Nickel/SEC purification. This finding is somewhat concerning because a postfusion F vaccine failed to prevent RSV illness in older adults[104]. Another key element in our study was the use of a pair of antibodies, prefusion site Ø-specific NAb D25[42] and postfusion site I-specific non-NAb ADI-14359[48], to probe fusion states of an RSV-F construct. Indeed, ADI-14359 in the ELISA confirmed the presence of postfusion F in Nickel/SEC-purified SC-TM-His_6 and 847A-His_6 samples. Overall, sc9-10 DS-Cav1[44] appeared to be the best of the four RSV-F designs. Our results also revealed two forms of RSV-F metastability: a tendency to undergo a rapid pre- to postfusion change and a tendency for prefusion trimers to open or dissociate in solution. The F_2-F_1 junction appeared to be another key contributor to metastability, in which sc9-10 DS-Cav1 differs the most from others in this region.

Systematic analyses of various RSV-F designs based on the $UFC_{R1\text{-}3}$ series (Fig. S11a, Table S9) allowed us to examine diverse design principles and identify alternative mutations to the interprotomer disulfide bond for maintaining prefusion RSV-F in a closed trimer. We arrived at the following key conclusions. First, an RSV-F construct with limited mutations can produce prefusion (albeit open) trimers with high yield and high purity, indicated by UFC_{R1}. The success of this "minimalist approach" provided a base construct to investigate RSV-F metastability and assess various solutions. Second, the buried acidic patch (^{485}DEFD^{488}) in β23 appears to trigger the prefusion RSV-F trimer to open because of the repulsive charge-charge interactions atop the trimeric α10 stalk. Either a hydrogen bond (NQ) or hydrophobic (L2) mutation could effectively maintain up to 76% of the RSV-F protein in a prefusion-closed conformation. Third, this acidic patch is critical to both forms of metastability and responds to remote mutations. For example, a hydrophobic (L2) mutation of this acidic patch likely results in breathing motions of RSV-F that transiently expose site I in both UFC_{R1} and UFC_{R2} contexts, suggesting that the two forms of metastability are intrinsically connected through this acidic patch. In addition, S46G and K465Q mutations in the UFC_{R2} base, more than 35 Å away from the acidic patch, drastically reduced the stabilizing effect of NQ and L2 mutations. Fourth, the β3-β4 hairpin in RSV-F, which is equivalent to $HR1_N$ (the fundamental cause of HIV-1 Env metastability[70,71]), has little impact on RSV-F metastability. The V185P (P2) mutation neither improved nor worsened any RSV-F properties in the UFC_{R1} and UFC_{R2} series. A similar pattern was observed for the interstrand disulfide bond (A177C-T189C), which was intended to lock the prefusion β3-β4 hairpin conformation. The extensive crystallographic analyses, in concert with other experimental approaches, validated our hypotheses on structural designs and RSV-F metastability at the atomic level.

Position-specific crosslinking presents another alternative, in addition to our "acidic patch" mutations, to the interprotomer disulfide bond for maintaining prefusion RSV-F in the closed form. Gidwani et al. successfully introduced two dityrosine (DT) bonds at the protomer interface[97], compared to a single interprotomer disulfide bond in the sc9-10 DS-Cav1 construct[44]. However, crosslinking in the Gidwani et al. study occurred at positions that are in the vicinity of site Ø and the site IV-V interface. As a result, the two DT bonds may alter the local conformation and occlude antibody access to these two critical neutralizing epitopes. The negative impact of interprotomer covalent bonds on antigenicity was evident from RSV-F binding to ADI-19425[48] and nanobody VHH-L66[83,84]. Notably, UFC_{R2}-iSS-P2-NQ and sc9-10 DS-Cav1 showed similar low binding to ADI-19425 and VHH-66L compared to UFC_{R1}-P2-NQ, likely due to the interprotomer disulfide bond in these two constructs. Thus, the effectiveness of engineered covalent bonds in controlling RSV-F metastability could only be achieved at the price of altered antigenicity.

Despite structural similarity to RSV-F, hMPV-F appears to not be confined by the same metastability principles, presenting a new challenge for antigen design and potentially explaining the suboptimal outcomes for recent hMPV-F designs[60–62]. First, RSV-F and hMPV-F differ significantly around the F_2-F_1 region, with a p27 peptide and double cleavage site in RSV-F *vs.* lack of the p27 peptide and a single cleavage site in hMPV-F, respectively, resulting in different sensitivity of the prefusion F design to truncation or linkage in the F_2-F_1 region. In our base design, UFC_{M1} (Fig. S11b), a short truncation at the F_2 C-terminus coupled with a G_6 linker resulted in prefusion-open trimers. However, a larger truncation in the F_2-F_1 region would produce postfusion hMPV-F trimers, as demonstrated by v3B_Δ18 and v3B_Δ15[60]. Second, unlike RSV-F, for which the P2 mutation displays no visible effect, the equivalent mutation (A185P) improves the expression of prefusion hMPV-F (albeit being open trimers). Third, unlike RSV-F, which contains an acidic patch essential to metastability, hMPV-F has a non-acidic ^{454}DQFN^{457} segment in β23, suggesting a different mechanism to trigger the prefusion trimer to open. Fourth, a well-placed interprotomer disulfide bond in UFC_{M1}-P2-iSS could effectively lock hMPV-F in a prefusion-closed trimer, but our attempt to replace iSS with a non-covalent interaction proved unsuccessful, resulting in a mixture of F species in UFC_{M1}-P2-F_2C-VL. Compared with the two recent designs[60,61], UFC_{M1}-P2-iSS offers a simple and robust construct for future development of effective hMPV-F vaccines (Table S9). However, the fundamental causes of hMPV-F metastability remain unclear. Nevertheless, our study indicates that the site Ø-specific NAb ADI-61026[65] provides an excellent probe for validating prefusion hMPV-F constructs as D25 did for the prefusion RSV-F design in the previous studies[43,44]. An ADI-61026 column may be generated for the

tag-free purification of prefusion hMPV-F, similar to the use of D25 in RSV-F purification.

The biopanning of a phage antibody library provided a direct in vitro approach to evaluate our top RSV-F design. Our hypothesis was that a prefusion-closed RSV-F trimer should select out both prefusion- and trimer-specific NAbs from a human antibody library that contains infection-induced RSV NAbs. Indeed, this was confirmed by our functional and structural characterization of a subset of scFv clones. A4 represents a "public" antibody lineage targeting a prefusion-specific epitope that overlaps sites Ø and V like RSD5[51], showing the highest IgG potency on par with MEDI8897 (Nirsevimab)[88]. D1 and F3 are MPE8-like NAbs directed to site III at the protomer interface[63], with F3 IgG demonstrating comparable potency to D25 against RSV[42] and 10-times higher potency than MPE8 against hMPV. We performed a mouse immunization study to assess antibody responses to various RSV-F and hMPV-F constructs. Overall, our serological analysis revealed a strong and positive correlation between binding and NAb responses. Among all RSV-F constructs, DS-Cav1[43] and SC-TM[33] elicited the lowest EC_{50} and ID_{50} titers at all timepoints, which correlated with trimer dissociation and the presence of postfusion F, respectively. The second-generation sc9-10 DS-Cav1 elicited the highest binding antibody and NAb titers. For our four RSV-F constructs, serum binding and NAb responses correlated with their in vitro and structural properties, thus confirming our design hypotheses. Within our three hMPV-F constructs, UFC_{MI}-P2-iSS elicited the most potent NAb responses with the highest ID_{50} titers at all timepoints, stressing the importance of a prefusion-closed conformation to NAb elicitation. Interestingly, some RSV-F-immunized mouse samples showed heterologous NAb responses against hMPV.

Our future studies may focus on the following directions. First, more in-depth examinations of metastability, as well as construct optimization, are required for hMPV-F. The introduction of an inter-protomer disulfide bond led to a lower trimer yield for UFC_{MI}-P2-iSS. Thus, it remains imperative to understand the causes of hMPV-F metastability and identify alternative mutations to maintain a prefusion-closed hMPV-F trimer. Second, single-cell antibody isolation, repertoire profiling, lineage tracing, and epitope mapping may be combined to delineate vaccine-elicited B-cell responses targeting diverse epitopes on the F protein (e.g., site Ø[42,65]) and the cross-pneumovirus epitope recognized by MPE8[63]. Such integrated analysis was demonstrated in our previous SARS-CoV-2 vaccine study[94]. Third, the optimized RSV-F and hMPV-F trimers can be displayed on our single-component, self-assembling protein nanoparticles (1c-SApNPs) to further improve immunogenicity and NAb elicitation. DS-Cav1 has been displayed on protein NPs for vaccine development[75,76]. We successfully designed 1c-SApNP vaccines for HIV-1[70,95,105], HCV[106], EBOV[69], SARS-CoV-2[68,94], and influenza[79]. Lastly, a bivalent RSV-F/hMPV-F vaccine may warrant careful evaluation. Although monovalent immunogens did not elicit heterologous NAb responses in our mouse study, a combination of optimized RSV-F and hMPV-F UFC trimers might generate an effective cross-pneumovirus NAb response.

Methods

Design, expression, and purification of RSV-F and hMPV-F

The amino acid sequences of RSV-F and hMPV-F were based on subtype A (strain A2, UniProt ID: P03420) and strain NL/1/00 (A1 sublineage, UniProt ID: Q1A2Z0), respectively. Structural modeling was performed using UCSF Chimera v1.13 software. All redesigned RSV-F and hMPV-F constructs were subcloned into a CMV/R vector and transiently expressed in ExpiCHO cells (Thermo Fisher, catalog no. A29133) as previously reported[69,95]. The cells were thawed and incubated with ExpiCHO™ Expression Medium (Thermo Fisher) in a shaker incubator at 37 °C, 135 rpm, and 8% CO_2. The cells were allowed to reach a cell density of 1×10^7/ml. On the day of transfection, the cells were diluted to 6×10^6/ml in ExpiCHO™ Expression Medium, after which ExpiFectamine™ CHO/plasmid DNA complexes were prepared for 25-ml transfection according to the manufacturer's instructions. For all RSV-F and hMPV-F constructs tested in this study, 25 µg F antigen plasmid and 80 µl of ExpiFectamine™ CHO reagent were mixed in 1.9 ml of cold OptiPRO™ medium (Thermo Fisher). After the first feed on day 1, ExpiCHO cells were further cultured in a shaker incubator at 32 °C, 120 rpm, and 8% CO_2 following the Max Titer protocol, with an additional feed on day 5 (Thermo Fisher). Culture supernatants were harvested 12–14 days after transfection, clarified by centrifugation at 3724 × *g* for 25 min, and filtered using a 0.45-µm filter (Millipore). Some RSV-F and hMPV-F constructs were purified using D25[42] and MPE8[63] NAb columns, whereas others were purified using Ni Sepharose excel resin (Nickel, Cytiva) as an alternative approach. For NAb columns, bound proteins were eluted three times, each with 5 ml of 0.2 M glycine (pH 2.2) and neutralized with 0.5 ml of Tris-Base (pH 9.0), and then exchanged into phosphate-buffered saline (PBS; pH 7.2). For Nickel columns, bound proteins were eluted twice, each with 15 ml of 0.5 M imidazole, and then exchanged into Tris-buffered saline (TBS; pH 7.2). The obtained RSV-F and hMPV-F proteins were further purified by size exclusion chromatography (SEC) using a Superdex 200 Increase 10/300 GL column (Cytiva) mounted on an ÄKTA pure system (Cytiva) under PBS buffer conditions. The trimer fractions were collected without further concentration. All SEC data were collected using UNICORN 7.5 software. The protein concentrations were calculated by measuring UV_{280} with theoretical extinction coefficients determined based on amino acid compositions using ProtParam on the ExPASy server[107]. All proteins were frozen down in liquid nitrogen and stored at −80 °C until further analysis.

Antibody expression and purification

All antibodies in IgG and Fab forms in this study were transiently expressed in ExpiCHO cells (Thermo Fisher). For IgGs and Fabs, 12–14 days post-transfection, the cells were centrifuged at 3724 × *g* for 25 min, and the supernatants were filtered using a 0.45-µm filter (Millipore). IgGs were further purified using protein A affinity resin (Cytiva) and eluted in 0.3 M citric acid (pH 3.0), and Fabs were purified using protein G affinity resin (Cytiva) and eluted in 0.2 M glycine (pH 2.0). The pH of the elution was immediately titrated to a neutral pH of 7.0 by the addition of 2 M Tris-Base (pH 9.0). The eluate was concentrated and exchanged into phosphate buffered saline (PBS) using an Amicon 10 kDa filter (Millipore). The antibody concentration was quantified by UV_{280} absorption with theoretical extinction coefficients.

Phage library-derived scFv-His and scFv-Fc antibodies were all transiently expressed in HEK293F (293F) cells using FreeStyle™ 293 Expression Medium. Briefly, HEK293F cells were thawed and incubated with FreeStyle™ 293 Expression Medium (Life Technologies, Carlsbad, CA, USA) in a shaker incubator at 37 °C at 135 rpm with 8% CO_2. When the cells reached a density of 2.0×10^6/ml, expression medium was added to reduce the cell density to 1.0×10^6/ml for polyethyleneimine (PEI; Polysciences) transfection. For 50-ml HEK293F transfection, 45 µg expression plasmid in 1.25 ml of Opti-MEM transfection medium (Life Technologies) was mixed with 1.25 ml of OptiMEM containing 0.5 ml of PEI-MAX (1.0 mg/ml). After 25 min of incubation, the DNA-PEI-MAX complex was added to HEK293F cells. Culture supernatants were harvested 5 days after transfection and centrifuged at 3724 × *g* for 15 min. Nickel and protein A resins were then used to purify scFv-His and scFv-Fc antibodies, respectively, from the clarified supernatant. Protein was then concentrated and buffer-exchanged into PBS using an Amicon 10 kDa filter. Purified antibodies were quantified using NanoDrop and stored at -80 °C until use.

Crosslinking of RSV-F and hMPV-F trimers in SDS-PAGE

SEC-purified RSV-F and hMPV-F proteins were crosslinked by disuccinimidyl glutarate (DSG) (Thermo Scientific, catalog no. 20593) and analyzed by SDS-PAGE under reducing conditions. Briefly, 5 µg of each

protein was prepared in 20 µl of PBS and mixed with 5 µl of 25 mM DSG in dimethylsulfoxide (DMSO). The mixture was incubated at room temperature for 30 min before the addition of 1.25 µl of quench buffer (1 M Tris-HCl, pH 7.0) and further incubated for 10 min. Next, 5 µl of 6× loading buffer was added to the sample and heated at 100 °C for 5 min. Thereafter, 12 µl of sample was loaded into 4–20% Mini-PROTEAN TGX™ Precast Gels (Bio-Rad). SDS-PAGE gels were then run for 50 min at 150 V in 1× Tris/glycine/SDS running buffer (Bio-Rad, catalog no. 1610732). Lastly, the gels were stained using InstantBlue Coomassie protein stain (Abcam) for 2 h and imaged by a ChemiDoc MP Imaging System (Bio-Rad).

Differential scanning calorimetry

Thermal melting curves of all RSV-F and hMPV-F proteins following antibody/Nickel column and SEC purification were obtained from a MicroCal PEAQ-DSC Man instrument (Malvern). Briefly, purified proteins in PBS buffer were adjusted to 1–5 µM before analysis. Melting was probed at a scan rate of 60 °C/h from 20 °C to 100 °C. Data processing, including buffer correction, normalization, and baseline subtraction, was conducted using MicroCal PEAQ-DSC software. Gaussian fitting was performed using GraphPad Prism 10.0.2 software.

Enzyme-linked immunosorbent assay (ELISA)

Costar™ 96-well, high-binding, flat-bottom, half-area plates (Corning) were first coated with 50 µl of PBS containing 0.1 µg of the appropriate RSV-F and hMPV-F antigens. The plates were incubated overnight at 4 °C and then washed five times with PBST wash buffer containing PBS and 0.05% (v/v) Tween 20. Each well was then coated with 150 µl of blocking buffer consisting of PBS and 40 mg/ml blotting-grade blocker (Bio-Rad). The plates were incubated with the blocking buffer for 1 h at room temperature, and then washed five times with PBST wash buffer. For antigen binding, antibodies (in either IgG or scFv form) were diluted in blocking buffer to a maximum concentration of 10 µg/ml followed by a 10-fold dilution series. For each antibody dilution, a total volume of 50 µl was added to the appropriate wells. For mouse sample analysis, serum was diluted 40-fold in blocking buffer and subjected to a 10-fold dilution series. For each sample dilution, a total volume of 50 µl was added to the wells. Each plate was incubated for 1 h at room temperature and then washed five times with PBST wash buffer. For antibody binding, a 1:5000 dilution of goat anti-human IgG antibody (Jackson ImmunoResearch Laboratories) or for mouse sample analysis, a 1:3000 dilution of horseradish peroxidase (HRP)-conjugated goat anti-mouse IgG antibody (Jackson ImmunoResearch Laboratories) was then made in the PBST wash buffer, with 50 µl of this diluted secondary antibody added to each well. The plates were incubated with the secondary antibody for 1 h at room temperature and then washed six times with PBST wash buffer. Finally, the wells were developed with 50 µl of 3,3′,5,5′-tetramethylbenzidine (TMB; Life Sciences) for 3–5 min before stopping the reaction with 50 µl of 2 N sulfuric acid. The plates were immediately read on a BioTek Synergy plate reader at a wavelength of 450 nm. EC_{50} values were then calculated from full curves using GraphPad Prism 10.0.2 software. When antibody binding signals (OD_{450}) were lower than 0.5, the binding was considered weak, and the EC_{50} values were set to 10 µg/ml in Figs. 1e, 2f, 4f to facilitate EC_{50} plotting and comparison.

Biolayer interferometry

Antigenic profiles of RSV-F and hMPV-F were measured using Octet RED96 (FortéBio, Pall Life Sciences) against a panel of 10 antibodies for RSV-F and four antibodies for hMPV-F, all in IgG forms. All assays were performed with agitation set to 1000 rpm in FortéBio 1× kinetic buffer. The final volume for all solutions was 200 µl per well. Assays were performed at 30 °C in solid black 96-well plates (Geiger Bio-One). For all antigens, 5 µg/ml antibody in 1× kinetic buffer was loaded onto the surface of anti-human Fc Capture Biosensors (AHC) for 300 s. Next, a 2-fold concentration gradient of antigen, starting at 600 nM, was used in a dilution series of six. A 60-s biosensor baseline step was applied before the analysis of association of the antibody on the biosensor to the antigen in solution for 200 s. Dissociation of the interaction was followed for 300 s, after which the correction of baseline drift was performed by subtracting the mean value of shifts recorded for controls: a sensor loaded with antibody + no antigen and a sensor without an antibody + an antigen. Octet data were processed by FortéBio's data acquisition software version 8.1. Peak signals at the highest antigen concentration were summarized in a matrix and color-coded accordingly to allow comparisons between different constructs. Experimental data for each antigen-antibody pair were fitted with the binding equations describing a 1:1 interaction, and three datasets that showed the optimal fitting were then grouped to determine the K_{on} and K_D values.

Protein crystallization and data collection

Freshly purified RSV-F proteins were used for crystallization experiments using the sitting drop vapor diffusion method on a Cryschem M Plate (Hampton Research) with protein concentrations between 5 and 10 mg/ml. For hMPV-F UFC_{M1}-P2-iSS-foldon-His6 and RSV-F sc9-10 DS-Cav1-foldon complexes with A4 scFv, ~8 mg/ml protein was used for crystallization experiments using the sitting drop vapor diffusion method using our automated CrystalMation robotic system (Rigaku) at 20 °C at The Scripps Research Institute[108]. The reservoir solution details are listed in Table S8. Diffraction-quality crystals were obtained after 2 weeks at 20 °C. All RSV-F crystals were cryoprotected with a well solution containing 25% (*v/v*) ethylene glycol, mounted on a nylon loop, and flash cooled in liquid nitrogen. Diffraction data were collected for all RSV-F crystals at Stanford Synchrotron Radiation Lightsource (SSRL) beamlines 12-1 and 12-2 and processed with HKL-2000[109]. Diffraction data for all RSV-F designs were indexed in $P4_321$, hMPV-F UFC_{M1}-P2-iSS-foldon-His6 in I213, and the complex of UFC_{R2}-iSS-P2-NQ with A4 scFv in R32.

Structure determination and refinement

Structures of all RSV-F constructs were determined by molecular replacement using Phaser-MR from Phenix (version 1.19.2-4158)[110] and the sc9-10 DS-Cav1 structure (PDB ID: 5K6I) as a search model. The hMPV-F UFC_{M1}-P2-iSS-foldon-His_6 structure was determined by molecular replacement using the previously reported prefusion hMPV-F (PDB ID: 5WB0). The structure of UFC_{R2}-iSS-P2-NQ in complex with A4 scFv was determined by molecular replacement using the prefusion RSV-F in complex with RSD5 Fab (PDB ID: 6DC3). Polypeptide chains were manually adjusted into electron density using Coot[111], refined with phenix-refine[110], and validated using the wwPDB Validation System[112]. Carbohydrates were validated using Privateer in CCP4i[113,114] before and after refinement to detect structural abnormalities. The final data processing and refinement statistics are described in Tables S2-S4, S6, S7. All images for crystal structures shown in the figures were generated using PyMOL v2.3.4 software.

Negative-stain electron microscopy (nsEM)

The nsEM analysis of RSV-F and hMPV-F trimers, as well as their antibody-bound complexes, was performed by the Core Microscopy Facility at The Scripps Research Institute. Briefly, samples were prepared at a concentration of 0.008 mg/ml. Carbon-coated copper grids (400 mesh) were glow-discharged, and 8 µl of each sample was then adsorbed for 2 min. Next, excess sample was removed, and grids were negatively stained with 2% uranyl formate for 2 min. Excess stain was wicked away and the grids were allowed to dry. Samples were analyzed at 120 kV with a Talos L120C transmission electron microscope (TEM, Thermo Fisher), and images were acquired using a CETA 16 M CMOS camera under ×73,000 magnification at a resolution of 1.93 Å/pixel and defocus of 0.5–2 µm. Computational analysis of the imaging data was

performed using the high-performance computing core facility at The Scripps Research Institute. Briefly, the nsEM images were converted to the MRC format by EMAN2[115] for further processing by CryoSPARC v4.3.0[116]. Micrographs were contrast-transfer function (CTF)-corrected by patch CTF estimation. Particles were selected using Blob/template picker and later extracted with a box size of 130 pixel for 2D classification, with 80 and 260 Å used as the minimum and maximum particle sizes in blob picking. Three-dimensional (3D) models were generated by ab initio reconstruction and optimized by heterogeneous and homogeneous refinement. All nsEM and fitted structure images were generated by UCSF Chimera[117] and Chimera X[118–120].

Preparation and biopanning of a healthy donor antibody phage library

Peripheral blood mononuclear cells (PBMC) from 10 healthy donors were purchased from iXCells Biotechnologies (San Diego, CA) and used for scFv library construction following our previously described method[87]. Briefly, total RNA was extracted from ~10 million PBMCs for single-stranded cDNA synthesis using SuperScript™ IV (Invitrogen) with random hexamer and oligo(dT) 12–18 primers. Antibody heavy chain (HC) and light chain (LC) variable regions were obtained by polymerase chain reaction (PCR) using mixed HuJ reverse primers and separate HuV forward primers[87]. To generate HC-LC fragments, overlap PCR was performed in 25 × 50 µl reactions (10 cycles) with 50 ng of gel-purified HC and 50 ng of gel-purified LC (equal amounts of κ and λ LC) without primer. Subsequent PCR was performed in 50 × 50 µl reactions (15 cycles) with SfiI-F and SfiI-R primers using 100 ng of gel-purified HC-LC as a template to obtain full-length scFv inserts. The scFv inserts and phagemid vector, pAdLTM-20c (Antibody Design Labs), were then digested with SfiI and purified through gel extraction. The scFv DNA (256 ng) was ligated into the phagemid vector (400 ng) using the T4 Ligase Kit (New England BioLabs) in 25 × 40 µl reactions and incubated at 16 °C overnight. After purification, the phagemids were electroporated into phage-competent TG1 bacterial cells (Lucigen) with the MicroPulsuer™ system (Bio-Rad). Specifically, 1 µl of phagemid and 25 µl of competent cells were incubated in a 0.1 cm cuvette for electroporation with the preset program at 1.8 kV. The transformed bacteria were spread on 2YT agar plates supplemented with 100 µg/ml carbenicillin and 2% (w/v) glucose, which were then incubated at 37 °C overnight. Bacteria were then scraped from the plates for phage culture with the helper phage CM13 (Antibody Design Labs) for biopanning. The purified UFC_{R1}-P2-NQ trimer was conjugated with Dynabeads™ M-270 beads before biopanning. A total of four biopanning steps were performed, incorporating up to five washes in each step to eliminate phages that were either not bound or showed low affinity for the RSV-F trimer. Lastly, plasmids from each biopanning step were extracted from 50 ml of the bacterial suspension and used for the subsequent deep sequencing and bioinformatics analyses of scFv libraries.

Phage enzyme-linked immunosorbent assay

Phage ELISA was performed to select scFv clones reactive to sc9-10 DS-Cav1 using a previously described protocol[121]. Briefly, wells of Costar™ 96-well assay plates (Corning) were coated with 50 µl of PBS containing 0.2 µg sc9-10 DS-Cav1 and incubated overnight at 4 °C. The next day, the plates were washed five times with PBST wash buffer and blocked with 150 µl/well of nonfat milk blocking buffer for 1 h at room temperature. The plates were then washed five times, and 50 µl of scFv-displaying phage was added to the appropriate wells. Each plate was incubated for 1 h and then washed five times with PBST wash buffer. Next, a 1:5000 dilution of HRP-conjugated mouse anti-M13 antibody (Sino Biological) was made in the wash buffer, and 50 µl of diluted antibody was added to each well. The plates were incubated for 1 h and washed five times with PBST wash buffer. Finally, the wells were developed with 50 µl of TMB for 5 min before the reaction was stopped with 50 µl of 2 N sulfuric acid. The plate readout was performed as described above for the ELISA analysis of antigen-antibody interactions. RSV-F reactive scFv clones were subjected to Sanger sequencing (Eton Bioscience) to extract nucleotide sequences.

Next-generation sequencing (NGS) and bioinformatics analysis

Two pairs of primers were used to generate NGS libraries. To amplify HC fragments, a forward primer containing an A adaptor, an Ion Xpress™ barcode (Life Technologies), and a cloning site-targeting motif, and a reverse primer containing a P1 adaptor and a GS linker-targeting motif, were used (listed in Fig. S8f). To amplify V_L or V_K fragments, a forward primer containing a P1 adaptor and a GS linker-targeting motif, and a reverse primer containing an A adaptor, an Ion Xpress™ barcode (Life Technologies), and a cloning site-targeting motif were used (Fig. S8f). One scFv library at each step of the biopanning process (pre-panning, Pan-0, Pan-1, Pan-2, and Pan-4) would produce three antibody chain libraries (V_H, V_L, and V_K). Three antibody chain libraries from each biopanning step (with the same barcode) were then quantitated using a Qubit® 2.0 Fluorometer with the Qubit®dsDNA HS Assay Kit and pooled. Finally, the five pooled libraries were mixed at a ratio of 5:1:1:1:1 for further processing. Template preparation and Ion 530 chip loading were performed on Ion Chef using the Ion 520/530 Ext Kit, followed by a single NGS run on the Ion GeneStudio S5 system, as previously described[122]. The Antibodyomics 2.0 pipeline[122] was used to process the raw NGS data and determine distributions for germline gene usage, somatic hypermutation, germline divergence, and CDR3 length. The 2D identity-divergence plots were used to visualize selected scFv lineages in the context of the antibody library at each biopanning step. The CDR3 identity of 95% and a 1-residue error margin of CDR length calculation were used to identify potential somatic variants of a reference antibody clone. These variants are shown as orange dots on the 2D plots (Fig. 7f, Fig. S8h).

Animal immunizations and sample collection

We utilized a similar immunization protocol from our previous vaccine studies[79,94,95]. All animal experiments followed the Association for the Assessment and Accreditation of Laboratory Animal Care (AAALAC) guidelines and used protocols that were approved by the Institutional Animal Care and Use Committee (IACUC) of The Scripps Research Institute (TSRI). Six-week-old female and male BALB/c mice were purchased from The Jackson Laboratory and housed in ventilated cages in environmentally controlled rooms in the Immunology building of The Scripps Research Institute. For the immunogenicity study, the mice were injected at weeks 0, 3, 6, and 9 with 80 µl of antigen/adjuvant mix containing 10 µg of vaccine antigen in 40 µl of PBS and 40 µl of AddaVax adjuvant (InvivoGen). Intradermal immunization in mice was performed through injections into four footpads, each with 20 µl of antigen/adjuvant mix using a 29-gauge insulin needle under 3% isoflurane anesthesia with oxygen. Blood was drawn from the maxillary/facial vein 2 weeks after each immunization. Serum was isolated from blood after centrifuged at 13,200 × *g* for 10 min. Serum was then heat-inactivated at 56 °C for 30 min, and the supernatant was collected after centrifugation at 4300 × *g* for 10 min. Heat-inactivated serum was used in the antigen binding and neutralization assays to determine vaccine-induce antibody responses.

Virus production and neutralization assays

The propagation of viruses and microneutralization assays for RSV and hMPV were based on previous protocols with modification[98,123,124]. The following reagents were obtained from ViraTree: RSV-A2-GFP and hMPV-GFP (parental strain CAN97-83). For the propagation of RSV-A2-GFP, 3.0×10^6 HEp-2 cells (American Type Culture Collection [ATCC], catalog no. CCL-23) were plated in 100 cm cell culture dishes. The next day, the cells were washed twice with PBS and infected with a

multiplicity of infection (MOI) between 0.01 and 1 of RSV-A2-GFP for 2 h. Next, 10 ml of growth media (2.5% fetal bovine serum [FBS] in Dulbecco's Modified Eagle Medium [DMEM]) was added to the plates, which were then incubated for 5 days at 37 °C. On the day of harvest, cells were scraped, resuspended in viral growth media, and centrifuged at 3724 × *g* for 10 min at 4 °C. Equal volumes of viral supernatant and 50% (w/v) sucrose in PBS were combined, aliquoted, and frozen at -80 °C until use. For hMPV propagation, 3.0×10^6 VeroE6 cells (ATCC catalog no. CRL-1586) were plated in 100 cm cell culture dishes overnight. The next day, the cells were washed twice with PBS and infected with a MOI between 0.01 and 1 of hMPV-GFP for 1 h. Next, inoculum was removed before the addition of 10 ml of virus growth media consisting of serum-free DMEM, 0.2% (w/v) bovine serum albumin (BSA; VWR), and 1 µg/ml L-1-tosylamido-2-phenylethyl chloromethyl ketone (TPCK)-treated trypsin (Sigma Aldrich). Cells were incubated for 6 days at 37 °C. On the day of harvest, cells were scraped, resuspended in the viral growth media, and centrifuged at 3724 × *g* for 10 min. The supernatant was aliquoted and frozen at -80 °C until use. For neutralization assays, RSV-A2-GFP or hMPV-GFP was incubated with serial dilutions of heat-inactivated mouse serum in black, clear-bottom 96-well plates (Corning, catalog no. 3603) in DMEM containing 2.5% FBS or serum-free DMEM containing 10 µg/ml TPCK-treated trypsin, respectively, for 1 h at 37 °C. Assays were performed in duplicate with 3-fold dilutions of antibodies (scFv-Fc and IgG) starting at 0.1–10 µg/ml and mouse serum starting at a 1:300 dilution. For RSV-A2-GFP neutralization, after 1 h of virus/serum incubation, 1.5×10^4 VeroE6 cells in DMEM containing 2.5% FBS were then added to each well, after which the plates were incubated for 72 h. For hMPV-GFP neutralization, after virus/serum incubation, 1.5×10^4 VeroE6 cells in DMEM containing 2.5% FBS were added to each well, producing a final concentration of 5 µg/ml TPCK-treated trypsin and 1.25% FBS. The plates were incubated for 72 h at 37 °C. On the day of the readout, supernatant was removed from the plates, 100 µl of PBS was added to each well, and the plates were read for GFP on a BioTek Synergy plate reader using Gen5 software. Values from experimental wells were compared against wells containing virus only, with both subtracting background fluorescence from cell control wells. Dose-response neutralization curves were then fitted by nonlinear regression in GraphPad Prism 10.0.2 software, with the IC_{50} and ID_{50} values calculated with constraints set between 0% and 100% neutralization.

Statistical analysis

Data were collected from 10 mice per group in the immunization studies. All assays, including serum binding and live RSV and hMPV neutralization, were performed in duplicate. Different vaccine constructs, adjuvant-formulated RSV-F and hMPV-F immunogens, were compared using one-way analysis of variation (ANOVA), followed by Tukey's multiple comparison *post hoc* test. Statistical significance is indicated as the following in the figures: ns (not significant), $*p < 0.05$, $**p < 0.01$, $***p < 0.001$, and $****p < 0.0001$. The graphs were generated, and statistical analyses were performed using GraphPad Prism 10.0.2 software.

Reporting summary

Further information on research design is available in the Nature Portfolio Reporting Summary linked to this article.

Data availability

All data to understand and assess the conclusions of this research are available in the main text and Supplementary Materials. The structural data have been deposited in the Protein Data Bank (PDB, https://www.rcsb.org/), under accession codes 8W3E, 8W3F, 8W3G, 8W3H, 8W3I, 8W3J, 8W3K, 8W3L, 8W3N, 8W3O, 8W3P, 8W3Q, and 8W3R. The NGS datasets of human scFv phage libraries have been deposited in the NIH Sequence Read Archive (SRA, https://www.ncbi.nlm.nih.gov/sra), with the identifier PRJNA1177972. The authors declare that the data supporting the findings of this study are available within the article and its Supplementary Information files. Source data are provided with this paper.

References

1. Borchers, A. T., Chang, C., Gershwin, M. E. & Gershwin, L. J. Respiratory syncytial virus - A comprehensive review. *Clin. Rev. Allergy Immunol.* **45**, 331–379 (2013).
2. Schildgen, V. et al. Human metapneumovirus: lessons learned over the first decade. *Clin. Microbiol. Rev.* **24**, 734–754 (2011).
3. Falsey, A. R., Hennessey, P. A., Formica, M. A., Cox, C. & Walsh, E. E. Respiratory syncytial virus infection in elderly and high-risk adults. *N. Engl. J. Med.* **352**, 1749–1759 (2005).
4. Stockman, L. J., Curns, A. T., Anderson, L. J. & Fischer-Langley, G. Respiratory syncytial virus-associated hospitalizations among infants and young children in the United States, 1997-2006. *Pediatr. Infect. Dis. J.* **31**, 5–9 (2012).
5. Shi, T. et al. Global, regional, and national disease burden estimates of acute lower respiratory infections due to respiratory syncytial virus in young children in 2015: a systematic review and modelling study. *Lancet* **390**, 946–958 (2017).
6. Alonso, J. A. N. et al. RSV: perspectives to strengthen the need for protection in all infants. *Emerg. Themes Epidemiol.* **18**, 15 (2021).
7. van den Hoogen, B. G. et al. A newly discovered human pneumovirus isolated from young children with respiratory tract disease. *Nat. Med.* **7**, 719–724 (2001).
8. Shi, T., McLean, K., Campbell, H. & Nair, H. Aetiological role of common respiratory viruses in acute lower respiratory infections in children under five years: A systematic review and meta-analysis. *J. Glob. Health* **5**, 122–131 (2015).
9. Boivin, G. et al. An outbreak of severe respiratory tract infection due to human metapneumovirus in a long-term care facility. *Clin. Infect. Dis.* **44**, 1152–1158 (2007).
10. Falsey, A. R., Erdman, D., Anderson, L. J. & Walsh, E. E. Human metapneumovirus infections in young and elderly adults. *J. Infect. Dis.* **187**, 785–790 (2003).
11. Papenburg, J. et al. Comparison of risk factors for human metapneumovirus and respiratory syncytial virus disease severity in young children. *J. Infect. Dis.* **206**, 178–189 (2012).
12. Boivin, G. et al. Virological features and clinical manifestations associated with human metapneumovirus: A new paramyxovirus responsible for acute respiratory-tract infections in all age groups. *J. Infect. Dis.* **186**, 1330–1334 (2002).
13. Boivin, G. et al. Human metapneumovirus infections in hospitalized children. *Emerg. Infect. Dis.* **9**, 634–640 (2003).
14. McAdam, A. J. et al. Human metapneumovirus in children tested at a tertiary-care hospital. *J. Infect. Dis.* **190**, 20–26 (2004).
15. Mullins, J. A. et al. Human metapneumovirus infection among children hospitalized with acute respiratory illness. *Emerg. Infect. Dis.* **10**, 700–705 (2004).
16. El Chaer, F. et al. Burden of human metapneumovirus infections in patients with cancer: risk factors and outcomes. *Cancer* **123**, 2329–2337 (2017).
17. Godet, C. et al. Human metapneumovirus pneumonia in patients with hematological malignancies. *J. Clin. Virol.* **61**, 593–596 (2014).
18. Divarathna, M. V. M., Rafeek, R. A. M. & Noordeen, F. A review on epidemiology and impact of human metapneumovirus infections in children using TIAB search strategy on PubMed and PubMed Central articles. *Rev. Med. Virol.* **30**, e2090 (2020).
19. Cuevas, L. E. et al. Human metapneumovirus and respiratory syncytial virus, Brazil. *Emerg. Infect. Dis.* **9**, 1626–1628 (2003).
20. Li, Y., Pillai, P., Miyake, F. & Nair, H. The role of viral co-infections in the severity of acute respiratory infections among children

infected with respiratory syncytial virus (RSV): A systematic review and meta-analysis. *J. Glob. Health* **10**, 010426 (2020).
21. Collins, P. L., Fearns, R. & Graham, B. S. Respiratory syncytial virus: Virology, reverse genetics, and pathogenesis of disease. *Curr. Top. Microbiol. Immunol.* **372**, 3–38 (2013).
22. McLellan, J. S., Ray, W. C. & Peeples, M. E. Structure and function of respiratory syncytial virus surface glycoproteins. *Curr. Top. Microbiol. Immunol.* **372**, 83–104 (2013).
23. Magro, M. et al. Neutralizing antibodies against the preactive form of respiratory syncytial virus fusion protein offer unique possibilities for clinical intervention. *Proc. Natl Acad. Sci. Usa.* **109**, 3089–3094 (2012).
24. Capella, C. et al. Prefusion F, postfusion F, G antibodies, and disease severity in infants and young children with acute respiratory syncytial virus infection. *J. Infect. Dis.* **216**, 1398–1406 (2017).
25. Ngwuta, J. O. et al. Prefusion F-specific antibodies determine the magnitude of RSV neutralizing activity in human sera. *Sci. Transl. Med.* **7**, 309ra162 (2015).
26. Gilman, M. et al. Rapid profiling of RSV antibody repertoires from the memory B cells of naturally infected adult donors. *Sci. Immunol.* **1**, eaaj1879 (2016).
27. Battles, M. B. & McLellan, J. S. Respiratory syncytial virus entry and how to block it. *Nat. Rev. Microbiol.* **17**, 233–245 (2019).
28. Melero, J. A., Mas, V. & McLellan, J. S. Structural, antigenic and immunogenic features of respiratory syncytial virus glycoproteins relevant for vaccine development. *Vaccine* **35**, 461–468 (2017).
29. Banerjee, A. et al. Structural basis for ultrapotent antibody-mediated neutralization of human metapneumovirus. *Proc. Natl Acad. Sci. Usa.* **119**, e2203326119 (2022).
30. Zimmer, G., Budz, L. & Herrler, G. Proteolytic activation of respiratory syncytial virus fusion protein - Cleavage at two furin consensus sequences. *J. Biol. Chem.* **276**, 31642–31650 (2001).
31. González-Reyes, L. et al. Cleavage of the human respiratory syncytial virus fusion protein at two distinct sites is required for activation of membrane fusion. *Proc. Natl Acad. Sci. USA* **98**, 9859–9864 (2001).
32. Gilman, M. S. A. et al. Characterization of a prefusion-specific antibody that recognizes a quaternary, cleavage-dependent epitope on the RSV fusion glycoprotein. *PLoS Pathog.* **11**, e1005035 (2015).
33. Krarup, A. et al. A highly stable prefusion RSV F vaccine derived from structural analysis of the fusion mechanism. *Nat. Commun.* **6**, 8143 (2015).
34. Shirogane, Y. et al. Efficient multiplication of human metapneumovirus in Vero cells expressing the transmembrane serine protease TMPRSS2. *J. Virol.* **82**, 8942–8946 (2008).
35. Battles, M. B. et al. Structure and immunogenicity of pre-fusion-stabilized human metapneumovirus F glycoprotein. *Nat. Commun.* **8**, 1528 (2017).
36. Ruckwardt, T. J., Morabito, K. M. & Graham, B. S. Immunological lessons from respiratory syncytial virus vaccine development. *Immunity* **51**, 429–442 (2019).
37. Mejias, A., Garcia-Maurino, C., Rodriguez-Fernandez, R., Peeples, M. E. & Ramilo, O. Development and clinical applications of novel antibodies for prevention and treatment of respiratory syncytial virus infection. *Vaccine* **35**, 496–502 (2017).
38. Griffin, M. P. et al. Safety, tolerability, and pharmacokinetics of MEDI8897, the respiratory syncytial virus prefusion F-targeting monoclonal antibody with an extended half-life, in healthy adults. *Antimicrob. Agents Chemother.* **61**, e01714–e01716 (2017).
39. Wilkins, D. et al. Durability of neutralizing RSV antibodies following nirsevimab administration and elicitation of the natural immune response to RSV infection in infants. *Nat. Med.* **29**, 1172–1129 (2023).
40. Graham, B. S., Gilman, M. S. A. & McLellan, J. S. Structure-based vaccine antigen design. *Annu. Rev. Med.* **70**, 91–104 (2019).
41. Graham, B. S. The journey to RSV vaccines - heralding an era of structure-based design. *N. Engl. J. Med.* **388**, 579–581 (2023).
42. McLellan, J. S. et al. Structure of RSV fusion glycoprotein trimer bound to a prefusion-specific neutralizing antibody. *Science* **340**, 1113–1117 (2013).
43. McLellan, J. S. et al. Structure-based design of a fusion glycoprotein vaccine for respiratory syncytial virus. *Science* **342**, 592–598 (2013).
44. Joyce, M. G. et al. Iterative structure-based improvement of a fusion-glycoprotein vaccine against RSV. *Nat. Struct. Mol. Biol.* **23**, 811–820 (2016).
45. Che, Y. et al. Rational design of a highly immunogenic prefusion-stabilized F glycoprotein antigen for a respiratory syncytial virus vaccine. *Sci. Transl. Med.* **15**, eade6422 (2023).
46. Tian, D. et al. Structural basis of respiratory syncytial virus subtype-dependent neutralization by an antibody targeting the fusion glycoprotein. *Nat. Commun.* **8**, 1877 (2017).
47. Mousa, J. J., Kose, N., Matta, P., Gilchuk, P. & Crowe, J. E. Jr. A novel pre-fusion conformation-specific neutralizing epitope on the respiratory syncytial virus fusion protein. *Nat. Microbiol.* **2**, 16271 (2017).
48. Goodwin, E. et al. Infants infected with respiratory syncytial virus generate potent neutralizing antibodies that lack somatic hypermutation. *Immunity* **48**, 339–349.e5 (2018).
49. Tang, A. M. et al. A potent broadly neutralizing human RSV antibody targets conserved site IV of the fusion glycoprotein. *Nat. Commun.* **10**, 4153 (2019).
50. Gilman, M. S. A. et al. Transient opening of trimeric prefusion RSV F proteins. *Nat. Commun.* **10**, 2105 (2019).
51. Jones, H. G. et al. Alternative conformations of a major antigenic site on RSV F. *PLoS Pathog.* **15**, e1007944 (2019).
52. Mukhamedova, M. et al. Vaccination with prefusion-stabilized respiratory syncytial virus fusion protein induces genetically and antigenically diverse antibody responses. *Immunity* **54**, 769–780.e6 (2021).
53. Graham, B. S. Vaccine development for respiratory syncytial virus. *Curr. Opin. Virol.* **23**, 107–112 (2017).
54. Papi, A. et al. Respiratory syncytial virus prefusion F protein vaccine in older adults. *N. Engl. J. Med.* **388**, 595–608 (2023).
55. Melgar, M. et al. Use of respiratory syncytial virus vaccines in older adults: recommendations of the advisory committee on immunization practices - United States, 2023. *Morb. Mortal. Wkly. Rep.* **72**, 793–801 (2023).
56. Mazur, N. et al. Respiratory syncytial virus prevention within reach: the vaccine and monoclonal antibody landscape. *Lancet Infect. Dis.* **23**, e2–e21 (2023).
57. Langedijk, A. C. & Bont, L. J. Respiratory syncytial virus infection and novel interventions. *Nat. Rev. Microbiol.* **21**, 734–749 (2023).
58. Ruckwardt, T. J. The road to approved vaccines for respiratory syncytial virus. *npj Vaccines* **8**, 138 (2023).
59. Carvalho, T. mRNA vaccine effective against RSV respiratory disease. *Nat. Med.* **29**, 755–756 (2023).
60. Ou, L. et al. Structure-based design of a single-chain triple-disulfide-stabilized fusion-glycoprotein trimer that elicits high-titer neutralizing responses against human metapneumovirus. *PLoS Pathog.* **19**, e1011584 (2023).
61. Hsieh, C. L. et al. Structure-based design of prefusion-stabilized human metapneumovirus fusion proteins. *Nat. Commun.* **13**, 1299 (2022).
62. Stewart-Jones, G. B. E. et al. Interprotomer disulfide-stabilized variants of the human metapneumovirus fusion glycoprotein induce high titer-neutralizing responses. *Proc. Natl Acad. Sci. Usa.* **118**, e2106196118 (2021).

63. Wen, X. et al. Structural basis for antibody cross-neutralization of respiratory syncytial virus and human metapneumovirus. *Nat. Microbiol.* **2**, 16272 (2017).
64. Corti, D. et al. Cross-neutralization of four paramyxoviruses by a human monoclonal antibody. *Nature* **501**, 439–443 (2013).
65. Rappazzo, C. G. et al. Potently neutralizing and protective anti-human metapneumovirus antibodies target diverse sites on the fusion glycoprotein. *Immunity* **55**, 1710–1724.e8 (2022).
66. Huang, J., Diaz, D. & Mousa, J. J. Antibody recognition of the pneumovirus fusion protein trimer interface. *PLoS Pathog.* **16**, e1008942 (2020).
67. Rush, S. A. et al. Characterization of prefusion-F-specific antibodies elicited by natural infection with human metapneumovirus. *Cell Rep.* **40**, 111399 (2022).
68. He, L. et al. Single-component, self-assembling, protein nanoparticles presenting the receptor binding domain and stabilized spike as SARS-CoV-2 vaccine candidates. *Sci. Adv.* **7**, eabf1591 (2021).
69. He, L. et al. Single-component multilayered self-assembling nanoparticles presenting rationally designed glycoprotein trimers as Ebola virus vaccines. *Nat. Commun.* **12**, 2633 (2021).
70. He, L. et al. HIV-1 vaccine design through minimizing envelope metastability. *Sci. Adv.* **4**, eaau6769 (2018).
71. Kong, L. et al. Uncleaved prefusion-optimized gp140 trimers derived from analysis of HIV-1 envelope metastability. *Nat. Commun.* **7**, 12040 (2016).
72. Yang, X. Z. et al. Highly stable trimers formed by human immunodeficiency virus type 1 envelope glycoproteins fused with the trimeric motif of T4 bacteriophage fibritin. *J. Virol.* **76**, 4634–4642 (2002).
73. Yang, X. Z. et al. Modifications that stabilize human immunodeficiency virus envelope glycoprotein trimers in solution. *J. Virol.* **74**, 4746–4754 (2000).
74. Yang, X. Z., Farzan, M., Wyatt, R. & Sodroski, J. Characterization of stable, soluble trimers containing complete ectodomains of human immunodeficiency virus type 1 envelope glycoproteins. *J. Virol.* **74**, 5716–5725 (2000).
75. Marcandalli, J. et al. Induction of potent neutralizing antibody responses by a designed protein nanoparticle vaccine for respiratory syncytial virus. *Cell* **176**, 1420–1431.e17 (2019).
76. Swanson, K. A. et al. A respiratory syncytial virus (RSV) F protein nanoparticle vaccine focuses antibody responses to a conserved neutralization domain. *Sci. Immunol.* **5**, eaba6466 (2020).
77. McLellan, J. S. et al. Structural basis of respiratory syncytial virus neutralization by motavizumab. *Nat. Struct. Mol. Biol.* **17**, 248–250 (2010).
78. McLellan, J. S. et al. Structure of a major antigenic site on the respiratory syncytial virus fusion glycoprotein in complex with neutralizing antibody 101F. *J. Virol.* **84**, 12236–12244 (2010).
79. Braz Gomes, K. et al. Single-component multilayered self-assembling protein nanoparticles displaying extracellular domains of matrix protein 2 as a pan-influenza A vaccine. *ACS Nano* **17**, 23545–23567 (2023).
80. McLellan, J. S., Yang, Y., Graham, B. S. & Kwong, P. D. Structure of respiratory syncytial virus fusion glycoprotein in the postfusion conformation reveals preservation of neutralizing epitopes. *J. Virol.* **85**, 7788–7796 (2011).
81. Sanders, R. W. et al. A next-generation cleaved, soluble HIV-1 env trimer, BG505 SOSIP.664 gp140, expresses multiple epitopes for broadly neutralizing but not non-neutralizing antibodies. *PLoS Pathog.* **9**, e1003618 (2013).
82. Rutten, L. et al. Structure-based design of prefusion-stabilized filovirus glycoprotein trimers. *Cell Rep.* **30**, 4540–4550.e3 (2020).
83. Rossey, I. et al. Potent single-domain antibodies that arrest respiratory syncytial virus fusion protein in its prefusion state. *Nat. Commun.* **8**, 14158 (2017).
84. Ma, L. et al. Structural interrogation of a trimeric prefusion RSV fusion protein vaccine candidate by a camelid nanobody. *Vaccine* **41**, 3308–3316 (2023).
85. Wen, X. et al. Structure of the human metapneumovirus fusion protein with neutralizing antibody identifies a pneumovirus antigenic site. *Nat. Struct. Mol. Biol.* **19**, 461–463 (2012).
86. Bose, M. E. et al. Sequencing and analysis of globally obtained human respiratory syncytial virus A and B genomes. *PLoS One* **10**, 22 (2015).
87. He, L. et al. Hidden lineage complexity of glycan-dependent HIV-1 broadly neutralizing antibodies uncovered by digital panning and native-like gp140 trimer. *Front. Immunol.* **8**, 1025 (2017).
88. Zhu, Q. et al. A highly potent extended half-life antibody as a potential RSV vaccine surrogate for all infants. *Sci. Transl. Med.* **9**, eaaj1928 (2017).
89. Wu, H. et al. Development of motavizumab, an ultra-potent antibody for the prevention of respiratory syncytial virus infection in the upper and lower respiratory tract. *J. Mol. Biol.* **368**, 652–665 (2007).
90. Zhang, Q. et al. Potent and protective IGHV3-53/3-66 public antibodies and their shared escape mutant on the spike of SARS-CoV-2. *Nat. Commun.* **12**, 4210 (2021).
91. Voss, W. N. et al. Prevalent, protective, and convergent IgG recognition of SARS-CoV-2 non-RBD spike epitopes. *Science* **372**, 1108–1112 (2021).
92. Dejnirattisai, W. et al. Antibody evasion by the P.1 strain of SARS-CoV-2. *Cell* **184**, 2939–2954.e9 (2021).
93. Krissinel, E. & Henrick, K. Inference of macromolecular assemblies from crystalline state. *J. Mol. Biol.* **372**, 774–797 (2007).
94. Zhang, Y.-N. et al. Mechanism of a COVID-19 nanoparticle vaccine candidate that elicits a broadly neutralizing antibody response to SARS-CoV-2 variants. *Sci. Adv.* **7**, eabj3107 (2021).
95. Zhang, Y.-N. et al. Single-component multilayered self-assembling protein nanoparticles presenting glycan-trimmed uncleaved prefusion optimized envelope trimmers as HIV-1 vaccine candidates. *Nat. Commun.* **14**, 1985 (2023).
96. Crank, M. C. et al. A proof of concept for structure-based vaccine design targeting RSV in humans. *Science* **365**, 505–509 (2019).
97. Gidwani, S. V. et al. Engineered dityrosine-bonding of the RSV prefusion F protein imparts stability and potency advantages. *Nat. Commun.* **15**, 2202 (2024).
98. Sun, Y. & López, C. B. Preparation of respiratory syncytial virus with high or low content of defective viral particles and their purification from viral stocks. *Bio-protoc.* **6**, e1820 (2016).
99. Falsey, A. R., Formica, M. A. & Walsh, E. E. Microneutralization assay for the measurement of neutralizing antibodies to human metapneumovirus. *J. Clin. Virol.* **46**, 314–317 (2009).
100. Fischinger, S., Boudreau, C. M., Butler, A. L., Streeck, H. & Alter, G. Sex differences in vaccine-induced humoral immunity. *Semin. Immunopathol.* **41**, 239–249 (2019).
101. Klein, S. L. & Flanagan, K. L. Sex differences in immune responses. *Nat. Rev. Immunol.* **16**, 626–638 (2016).
102. Huang, J. C., Miller, R. J. J. & Mousa, J. J. J. A pan-pneumovirus vaccine based on immunodominant epitopes of the fusion protein. *Front. Immunol.* **13**, 941865 (2022).
103. Kampmann, B. et al. Bivalent prefusion F vaccine in pregnancy to prevent RSV illness in infants. *N. Engl. J. Med.* **388**, 1451–1464 (2023).
104. Falloon, J. et al. An adjuvanted, postfusion F protein-based vaccine did not prevent respiratory syncytial virus illness in older adults. *J. Infect. Dis.* **216**, 1362–1370 (2017).

105. He, L. et al. Presenting native-like trimeric HIV-1 antigens with self-assembling nanoparticles. *Nat. Commun.* **7**, 12041 (2016).
106. He, L. et al. Proof of concept for rational design of hepatitis C virus E2 core nanoparticle vaccines. *Sci. Adv.* **6**, eaaz6225 (2020).
107. Gasteiger E. et al. in *The Proteomics Protocols Handbook*, J. M. Walker, Ed. (Humana Press, Totowa, NJ, 2005), pp. 571-607.
108. Elsliger, M. A. et al. The JCSG high-throughput structural biology pipeline. *Acta Crystallogr. F: Struct. Biol. Commun.* **66**, 1137–1142 (2010).
109. Otwinowski, Z. & Minor, W. Processing of X-ray diffraction data collected in oscillation mode. *Methods Enzymol.* **276**, 307–326 (1997).
110. Liebschner, D. et al. Macromolecular structure determination using X-rays, neutrons and electrons: recent developments in Phenix. *Acta Crystallogr. D: Struct. Biol.* **75**, 861–877 (2019).
111. Emsley, P., Lohkamp, B., Scott, W. G. & Cowtan, K. Features and development of Coot. *Acta Crystallogr. D: Struct. Biol.* **66**, 486–501 (2010).
112. Berman, H., Henrick, K. & Nakamura, H. Announcing the worldwide Protein Data Bank. *Nat. Struct. Biol.* **10**, 980 (2003).
113. Agirre, J. et al. Privateer: software for the conformational validation of carbohydrate structures. *Nat. Struct. Mol. Biol.* **22**, 833–834 (2015).
114. Agirre, J. et al. The CCP4 suite: integrative software for macromolecular crystallography. *Acta Crystallogr. D: Struct. Biol.* **79**, 449–461 (2023).
115. Tang, G. et al. EMAN2: An extensible image processing suite for electron microscopy. *J. Struct. Biol.* **157**, 38–46 (2007).
116. Punjani, A., Rubinstein, J. L., Fleet, D. J. & Brubaker, M. A. cryoSPARC: Algorithms for rapid unsupervised cryo-EM structure determination. *Nat. Methods* **14**, 290–296 (2017).
117. Pettersen, E. F. et al. UCSF Chimera–a visualization system for exploratory research and analysis. *J. Comput. Chem.* **25**, 1605–1612 (2004).
118. Meng, E. C. et al. UCSF ChimeraX: tools for structure building and analysis. *Protein Sci.* **32**, e4792 (2023).
119. Pettersen, E. F. et al. UCSF ChimeraX: structure visualization for researchers, educators, and developers. *Protein Sci.* **30**, 70–82 (2021).
120. Goddard, T. D. et al. UCSF ChimeraX: meeting modern challenges in visualization and analysis. *Protein Sci.* **27**, 14–25 (2018).
121. Andris-Widhopf, J., Steinberger, P., Fuller, R., Rader, C. & Barbas, C. F. 3rd Generation of human scFv antibody libraries: PCR amplification and assembly of light- and heavy-chain coding sequences. *Cold Spring Harb. Protoc.* **2011**, pdb.prot065573 (2011).
122. Wen, G. P. et al. Quantitative evaluation of protective antibody response induced by hepatitis E vaccine in humans. *Nat. Commun.* **11**, 3971 (2020).
123. Raghunandan, R., Higgins, D. & Hosken, N. RSV neutralization assays - use in immune response assessment. *Vaccine* **39**, 4591–4597 (2021).
124. Biacchesi, S. et al. Infection of nonhuman primates with recombinant human metapneumovirus lacking the SH, G, or M2-2 protein categorizes each as a nonessential accessory protein and identifies vaccine candidates. *J. Virol.* **79**, 12608–12613 (2005).

Acknowledgements

Diffraction data were collected at the Stanford Synchrotron Radiation Lightsource (SSRL) beamlines 12-1 and 12-2. Use of the SSRL and Stanford Linear Accelerator Center (SLAC) National Accelerator Laboratory is supported by the U.S. Department of Energy, Office of Science, Office of Basic Energy Sciences under Contract No. DE-AC02-76SF00515. The SSRL Structural Molecular Biology Program is supported by the Department of Energy (DOE) Office of Biological and Environmental Research, and by the National Institutes of Health, National Institute of General Medical Sciences (P30GM133894). We thank V. Tong and M. Arends for proofreading the manuscript. This work was supported by Ufovax/SFP-2018-1013 (J.Z.).

Author contributions

Project design by Y.-Z.L., J.H., Y.-N.Z., K.B.G., L.H., and J.Z.; protein design by J.Z.; protein expression and purification by G.W., Y.-Z.L., and L.H.; EM analysis by Y.-Z.L., L.H., and J.Z.; crystal structures by Y.-Z.L., R.L.S., and I.A.W.; mouse immunization, sample collection, and serum binding analysis by Y.-N.Z.; live RSV and hMPV propagation and neutralization assay by G.W., K.B.G., and L.H.; manuscript written by Y.-Z.L., J.H., Y.-N.Z., K.B.G., S.A., L.H., and J.Z. All authors were asked to comment on the manuscript. The Scripps Research Institute manuscript number is 30254.

Competing interests

The authors declare the following competing interests: J.Z. serves as the Co-Founder, Interim Chief Scientific Officer, Consultant, and Scientific Advisory Board member of Uvax Bio, LLC, and holds associated financial interests. Other authors declare that they have no competing interests.

Additional information

Supplementary information The online version contains supplementary material available at https://doi.org/10.1038/s41467-024-54287-x.

Correspondence and requests for materials should be addressed to Jiang Zhu.

Peer review information *Nature Communications* thanks Bert Schepens, and the other, anonymous, reviewers for their contribution to the peer review of this work. A peer review file is available.